Competing Photo-Cleavage on Boron and at the *meso*-Position in BODIPY Photocages

Ivan Ljubić,[a]* Igor Sviben,[b] Vedran Brusar,[c] Katarina Zlatić,[b,d] Silvije Vdović,[c] Nikola Basarić[b]*

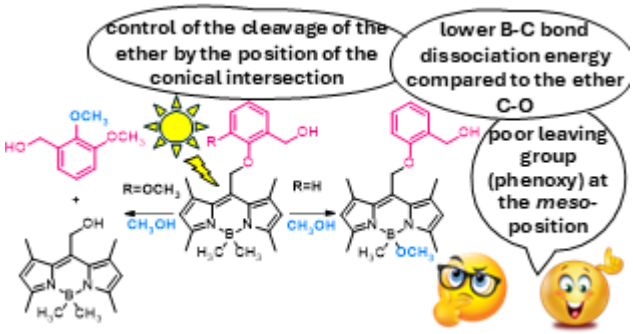
[a] Department of Physical Chemistry, Ruđer Bošković Institute, Bijenička cesta 54, 10 000 Zagreb, Croatia. E-mail: ivan.ljubic@irb.hr

[b] Department of Organic Chemistry and Biochemistry, Ruđer Bošković Institute, Bijenička cesta 54, 10 000 Zagreb, Croatia. E-mail: nbasaric@irb.hr

[c] Centre for Advanced Laser Techniques, Institute of Physics, Bijenička cesta 46, 10 000 Zagreb, Croatia.

[d] Current address: Institute of Organic Chemistry and Biochemistry of the Czech Academy of Sciences, Flemingovo náměstí 542/2, Prague 6, 160 00, Czech Republic.

TOC:



Abstract:

BODIPY photocages (photo-cleavable protective groups) have stirred interest because they can release biologically active cargo upon visible light excitation. We conducted combined theoretical and experimental investigations on selected BODIPY photocages to elucidate the mechanism of the competing photo-cleavage at the boron and *meso*-position. Based on the computations, the former reaction involves elongation of the B-C bond yielding a tight borenium cation and methyl anion. These ions are intercepted by CH_3OH enabling an efficient proton-coupled electron transfer (PCET) to produce the methane and isolated ether photoproducts. Singlet and triplet excited state lifetimes were measured in CH_3OH and CD_3OD to probe for the kinetic isotope effects (KIE). The resulting KIEs are small implying that the kinetic bottleneck is due to the C-B bond scission rather than the subsequent PCET. The introduction of methoxy group in the *meso*-phenoxy substituent redirects the photo-substitution toward the *meso*-position. The corresponding regiochemistry was explained

computationally. On elongating the C-O bonds in the S_1 state, it is found that the unproductive conical intersection is encountered much earlier for the alkyl-O bond than for the phenyl-O bond. The current findings are valuable for the rational design of new BODIPY photocages with tailored biological applications.

Key Words: BODIPY, photocages, photo-cleavage of the C-B bond, TD-DFT and CASSCF/CASPT2 computations

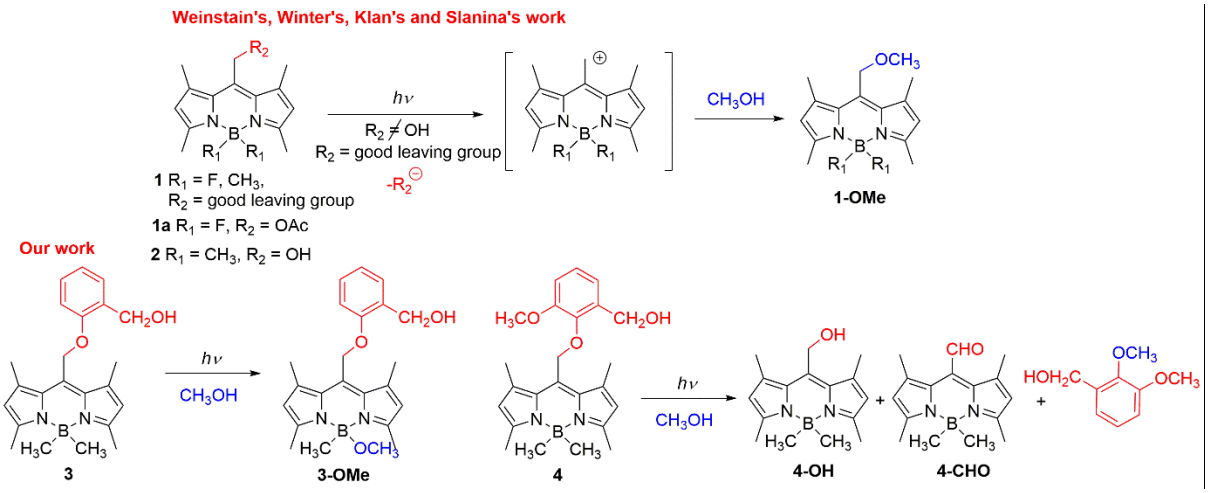
Introduction

From the introduction of click chemistry, the concept of building complex molecular structure from simple building blocks has expanded, particularly for the use in biological systems.[1] Furthermore, the development of photochemically controlled click reactions has allowed for spatial and temporal resolution of the site-specific building of complex molecular architecture with applications on surfaces or in bio-systems.[2] In addition to controlled building of more complex structures, researchers develop methodologies to selectively cleave molecules, the concept known as photo-clipping.[3] Such selective transformation of molecules into an active form in the controlled process at the desired location has been in the focus of photo-pharmacology,[4,5] which blossomed in the last two decades owing to the development of photo-cleavable protective groups, also known as photocages.[6,7] The chemistry of photocages has been reviewed on several occasions,[8,9,10,11,12,13,14] including recent developments of photocages that absorb visible light, which can penetrate tissues,[15] and have applications in biology.[16]

Among photocages that absorb visible light, BODIPY compounds have shown excellent performance,[17,18] leading to applications in medicine,[19,20] and super resolution microscopy in biology.[21,22,23,24] BODIPY is the trade name for 4,4-difluoro-4-bora-3a,4a-diaza-*s*-indacene derivatives,[25,26] fluorescent dyes characterized by exceptional spectroscopic and photophysical properties,[27,28] which can be easily tuned by simple structural modifications.[29,30] The design of BODIPY photocages[31,32,33] is based on computational prediction of photochemical formation of stable cations on the excited state surface, or unstable cations in the ground state via a conical intersection (CI).[34] Extensive structure-activity relationship and mechanistic studies of the photo-release reaction were performed[35,36,37] to find optimal BODIPY structure for the efficient and wavelength-selective release (also called photo-orthogonality).[36,38] The scope of the decaging was demonstrated on the eliminations of carboxylic acids,[32,35,36,37,38] halides,[35,37] CO,[39] H_2S,[40] phosphates,[37] alcohols and phenols,[41] and amines.[42]

Photo-release of substrates from BODIPY photocages is mostly considered to take place at the *meso*-methyl position via a heterolysis.[17,36] Thus, upon irradiation of BODIPY derivatives **1** in CH_3OH, bearing a good leaving group at the *meso*-methyl position, ethers **1-OMe** are formed via a cationic intermediate in the triplet state,[15] which however, has never been experimentally observed (Scheme 1).[17,35,36] Furthermore, photocleavage from carbon atoms other than the *meso*-methyl of the BODIPY chromophore have been reported,[43,44,45] but these reactions have not yet been extensively used as photocages. For the cleavage at the *meso*-position it is suggested that the heterolysis generally takes place via triplet excited state, and that it is more efficient if the fluorines are substituted by methyl groups.[35] Therefore, we

designed a new line of BODIPY compounds substituted at the *meso*-methyl group with a phenolic substituent, which was anticipated to eliminate and deliver quinone methides.[46] However, we found competing solvolysis reaction at the boron atom of the BODIPY, taking place at least ten times more efficiently than the elimination at the *meso*-position, unless the phenol was substituted with an OCH_3 group (Scheme 1). The photosolvolysis at the boron atom of BODIPY has been reported,[47,48,49] albeit the reaction mechanism has never been disclosed. Herein we report on photochemical reactivity and photophysical properties of compounds **2**-**4** as model compounds for important class of photocages.[17,18] A combination of theoretical approach with experiments, including irradiations, time-resolved fluorescence and transient spectroscopy with time-scale from femtoseconds to microseconds, was employed to unravel the photosolvolysis reaction mechanism and competing pathways at the *meso*-position and the boron atom. The major finding is that the photo-cleavage reaction on boron likely involves proton coupled electron transfer (PCET) and proceeds in a solvent-separated ion pair, without detectable intermediates en route. These mechanistic findings are important for the applications of BODIPY photocages, particularly in biology, since reactive intermediates may interact with different biological molecules. Furthermore, the knowledge on photo-decaging reaction mechanism is pivotal for the rational design of new generations of photocages.



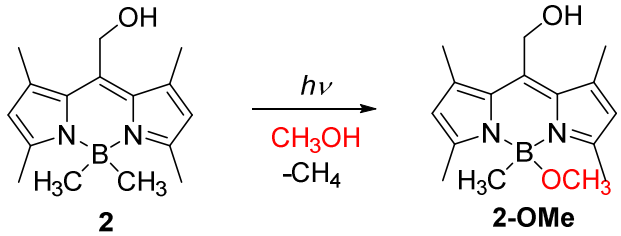
Scheme 1. Photolysis of BODIPY photocages with a good or poor (phenoxyl) leaving group at the *meso*-position from literature precedent.

Results

Irradiation Experiments

Photoreactivity of **3** and **4** in CH_3OH was reported to take place at the boron, or at the *meso*-position, respectively (Scheme 1).[46] Thus, upon irradiation of **3** and **4** in CH_3OH, the cleavage takes place giving **3-OMe** or **4-OH**, respectively, which were isolated and characterized. The yields of the isolated products in the photoreactions of **3** and **4** from literature precedent are reported in Table 1.[46] Note the unexpected ether bond cleavage in compound **4**, different from that anticipated from literature precedent.[31-42] Here we investigated the photochemical reactivity of **2** in CH_3OH in the solution purged with Ar or O_2, where it was expected that the O_2 would quench the triplet excited state resulting in lower

yield of the photoproduct. For the purpose of comparison, we irradiated also **3** under the same conditions. Photolysis of **2** in CH_3OH (3 h, visible light, for details see the SI) in Ar- and O_2-purged solution gave rise to the conversion of 28 and 27%, respectively. In the photoreaction only one photoproduct **2-OMe** was detected (Scheme 2). Under the same irradiation conditions, 1 h photolysis of **3** in Ar-purged solution proceeded with the conversion of 37%. Thus, the irradiation experiments indicated that the photomethanolysis of **3** is more efficient than for **2**. Furthermore, no quenching by O_2 is in accord with the reaction proceeding predominantly from the singlet excited state. Quantum yields of the photochemical reactions of **2**-**4** in CH_3OH were determined by using photolysis of **1a** as actinometer (Schemes 1 and S1, Φ_R = 0.0034).[35] The results are compiled in Table 1. The quantum yields for the photoreaction of **3** and **4** are 2.5 and 10 times higher than for **2**. To isolate the photoproduct **2-OMe** and characterize it by NMR, a larger quantity of **2** was irradiated (see Table 1 and Experimental).



Scheme 2. Photomethanolysis of **2**.

Table 1. Irradiation conditions (concentrations and irradiation times), isolated yields and the cleavage reaction quantum yields (Φ_R) for **1**-**3**.

Comp.	Irradiation conditions[a]	Isolated yields [b]	Φ_R[c]
2	3.7×10^{-3} M, 36 h	**2-OMe** (38%)	0.021 ± 0.007
3	5.0×10^{-3} M / 27 h [d]	**3-OMe** (35%) [d]	0.05 ± 0.02
4	3.3×10^{-3} M / 5 h [d]	**4-OH** (24 %) + **4-CHO** (11%)[d]	0.2 ± 0.1

[a] The irradiations were conducted in N_2 or Ar-purged CH_3OH solutions in quartz test tubes (15 mL each) in a Luzchem reactor equipped with 8 cool white lamps (each 8 W). [b] Isolable yields after chromatography, which are different from the HPLC ratio of products after small scale irradiations discussed above in the text. [c] The reaction quantum yields correspond to the photolyses in N_2-purged CH_3OH solutions ($c = 1 \times 10^{-3}$ M) upon 488 nm laser excitation. The photomethanolysis of **1a** was used as an actinometer (Φ_R = 0.0034).[35] [d] The data taken from ref. 46

To show that upon irradiation of **2** methane is formed as an elimination product, the irradiation of **2** was conducted in CD_3OD in a NMR tube (2 mg in 0.8 mL) over 4h. Immediately after the irradiation ^{1}H NMR spectrum was taken which showed a broad signal with unresolved coupling at $\delta \approx 0.2$ ppm whose intensity matched the decrease of the methyl signal at 0.16 ppm corresponding to the B-CH_3. It was tentatively assigned to the product CH_3D (it should appear as a triplet with J = 1.9 Hz)[50,51,52] formed from the B-CH_3 substituent and the CD_3OD solvent (see the spectrum in the SI).

Photophysical Properties of 1-3

To unravel mechanism of the photoreaction, we investigated the photophysical properties of **2**-**4**. The singlet excited state properties were probed by steady-state and time-resolved fluorescence in CH_3CN, where the molecules were anticipated to be photochemically stable and in CH_3OH (CD_3OD) where they are photo-reactive. The investigated BODIPY derivatives have absorption maxima in CH_3CN at ≈ 505-510 nm, and relatively strong emission with maximum at ≈ 520-530 nm and quantum yields of fluorescence Φ_F = 0.32-0.33 (Table 2).[46] The decays of fluorescence were measured by time-correlated single photon counting (TC-SPC). They were fit to sum of exponents revealing more complex photophysics. The computations indicated that the multiexponential decay is due to fluorescence from several vibrational states, since conformers or tautomers are not possible and S_1 is well-separated in energy from higher excited states (vide infra, computations).

Triplet excited states were investigated by nanosecond laser flash photolysis (LFP). Molar absorption coefficient of the triplet excited states and quantum yields of intersystem-crossing Φ_{ISC} were measured by singlet depletion method[53] and comparison of the signal intensity with the reference, zinc tetraphenylporphirin (Φ_{ISC} = 0.88).[54,55] Φ_{ISC} values are generally low (Table 1), and triplet excited state lifetimes are in microsecond time-scale. For all LFP data in CH_3CN see the SI. The low values of Φ_{ISC} are in accord with the photochemistry predominantly taking place from the singlet excited state, as indicated also by no quenching of the reaction by O_2. However, since the reactions are inefficient (Table 1), a parallel minor reaction pathway in the triplet excited state cannot be excluded.

Table 2. Photophysical properties of **1**-**3** in CH_3CN.

Compound	Φ_F (CH_3CN)[a]	τ (CH_3CN) / ns[b]	ε(430 nm)/$M^{-1}s^{-1}$ [c] Φ_{ISC} [d]	τ_T (CH_3CN)/μs [e]
2	0.32±0.01	2.11±0.07 (0.7) 3.4 ±0.2 (0.3)	18800±300 0.05±0.01	60±10
3	0.33±0.06	1.82±0.02 (0.7) 4.5 ±0.1 (0.3)	11600±400 0.07±0.01	60±10
4	0.33±0.03	1.83±0.03 (0.65) 4.83 ±0.08 (0.35)	14400±400 0.04±0.01	50±10

[a] Fluorescence quantum yields (Φ_f) were measured in CH_3CN using rhodamine B in CH_3OH (Φ_f = 0.66)[56] as a reference. The values taken from ref. 46 [b] Decay of fluorescence was measured by TC-SPC upon excitation at 445 nm. The values in parenthesis correspond to the contribution of decay component. Two decay components were tentatively assigned to the population of higher vibrational levels of electronically excited states. [c] The molar absorption coefficient of triplet excited state measured by depletion method. [d] Quantum yield of intersystem crossing (ISC) measured by use of zinc tetraphenylporphyrin as a reference (Φ_{ISC} = 0.88).[54,55] [e] Triplet excited state lifetimes.

Ultrafast Transient Absorption Experiments

To get deeper insight into the deactivation from the singlet excited state and potentially probe for the intermediates in the photolysis on the ultrashort time-scale, fs-TA measurements were performed for **2** in CH_3OH (Fig. 1). Upon excitation at 500 nm, within 100 fs, a transient

absorption was observed with a maximum at 360 nm, and the negative signal between 450-650 nm. With our sub-100 fs time resolution we were unable to observe any spectral changes on short time scales (additional measurement focused on the first few picoseconds is shown in the SI). The transient absorption at 360 nm was assigned to the excited state absorption of **2**(S_1) based on computation, and the negative signal corresponds to the ground state bleach of molecule **2**(S_0) and stimulated emission. Both signals decay over nanosecond time-scale. Positive signal decays with single 2.3 ns decay constant while negative signal in the region where stimulated emission dominates, above 520 nm, is best fitted using two time constants: 2.3 and 5.2 ns (Fig. 1b). Decay times from the fs-TA are in accord with the data obtained by TC-SPC. Thus, fs-TA did not reveal any intermediate with short decay time, which would be formed from **2**(S_1). The finding suggests that **2**(S_1) directly delivers methanolysis photoproducts without detectable intermediates en route, or that such intermediates have very short lifetimes (vide infra), or that they are not detectable due to inefficient photoreaction.

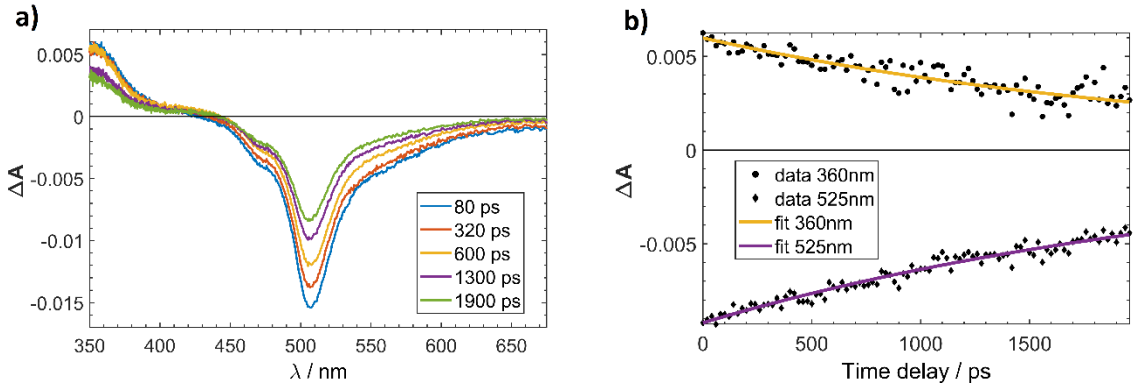


Fig. 1. (a) Spectral and (b) temporal dynamics obtained from fs-TA data for **2** in CH_3OH (c = 7.62×10^{-5} M). Pump fluence was set to 1.7 mJ/cm^2.

Photoreactivity in the Presence of Deuterated Solvent

The photoreactivity of **2**-**4** in CH_3OH is expected to affect their photophysical properties in that solvent (Table 3). Interestingly, Φ_F values are higher in CH_3OH than in CH_3CN, not in correlation with the photomethanolysis reactivity trend. This may be explained by the effect of protic solvent on the non-radiative decay channels through forming intermolecular H-bonds with the BODIPY molecules, and in that way slowing down the non-radiative decay channels. Moreover, residual inefficient triplet excited state reactivity cannot be excluded.

It was inferred that the methanolysis reaction involves the PCET step (vide infra), for which a large isotope effect is anticipated.[57] To additionally verify if the photomethanolysis reaction takes place mainly from the singlet excited states and via a PCET mechanism, fluorescence was measured in CH_3OH and CD_3OD, where the anticipated kinetic isotope effect (KIE) on reactions involving O-H/O-D cleavage would result in higher Φ_F and slower fluorescence decay in the deuterated solvent. However, the measured Φ_F values are the same, within experimental error. On the other hand, the KIE was observed for the decays of fluorescence. For compound **2**, the KIE with the value of 1.06 was observed for the fast decay component. For compounds **3** and **4**, both decay components live longer in deuterated solvent. Thus, the KIE values for **3** for the fast and slow components are 1.02 and 1.1, respectively. For **4**, the KIE values are 1.07 (fast) and 1.13 (slow component). Note that these KIE have low values,

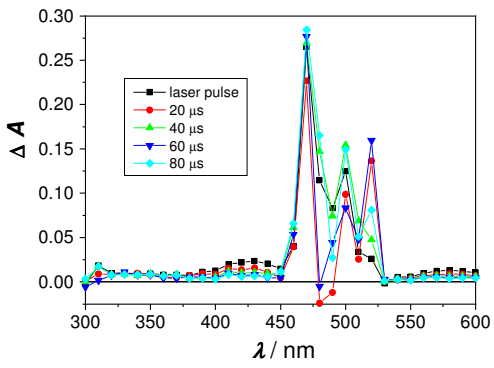
suggesting that they correspond to the secondary KIE; that is, the cleavage of the O-H/O-D bond is not the slowest step in the reaction mechanism. However, these small values of KIE are also in accord with the inefficient reaction taking place from singlet excited state, particularly for **2** and **3**.

Table 3. Quantum yields of fluorescence (Φ_F) and singlet excited state decay times (τ) for **2**-**4** measured in CH_3OH and CD_3OD.

Compound	Φ_F (CH_3OH)[a]	τ (CH_3OH) / ns [b]	Φ_F (CD_3OD)	τ (CD_3OD) / ns
2	0.46 ± 0.01	2.36 ± 0.03 (0.72) 5.2 ± 0.1 (0.28)	0.48 ± 0.01	2.50 ± 0.04 (0.77) 5.2 ± 0.2 (0.23)
3	0.43 ± 0.02	2.13 ± 0.02 (0.80) 5.2 ± 0.1 (0.20)	0.42 ± 0.04	2.17 ± 0.02 (0.77) 5.7 ± 0.1 (0.23)
4	0.29 ± 0.01	1.94 ± 0.03 (0.65) 4.4 ± 0.1 (0.35)	0.29 ± 0.02	2.08 ± 0.03 (0.63) 4.96 ± 0.09 (0.37)

[a] Φ_F was measured by use of rhodamine B in CH_3OH as a reference (Φ_F = 0.66).[56] Decay times were determined by TC-SPC. The values in parenthesis correspond to the weighted contribution of the decay component.

Due to low values of KIE for the fluorescence decay, LFP experiments in CH_3OH and CD_3OD were performed to probe for plausible inefficient photoreactivity in the triplet excited state and plausible long-lived intermediates that cannot be detected on short time-scale of fs-TA experiments. Comparison of the transient absorption spectra in CH_3CN (shown in the SI) and CH_3OH (Fig. 2) reveal no significant differences. The spectra are similar with an absorption band exhibiting maxima at ≈460 and ≈ 575 nm, which were assigned to the triplet excited state based on the quenching by O_2. Note that due to the strong signal of the ground state bleach and strong fluorescence of the sample which saturates the detector, the measurement in the 450-550 nm region is not reliable. Interestingly, the decays of the triplet excited states in CH_3CN and CH_3OH are similar. However, the triplets decay faster in CH_3OH than in CD_3OD (Table 4). The ratio of the triplet lifetimes reveals the KIE of 1.6 for **2** and 2.6 for **3**, which indicates that H-O/D-O bond breaking may be involved in the deactivation of molecules from the triplet excited state. Note, however, that these values of KIE are much lower than the ones typically reported for molecules undergoing PCET.[57] Nevertheless, the LFP experiments indicate that triplet excited states, while inefficiently populated, may still be involved in the photomethanolysis.



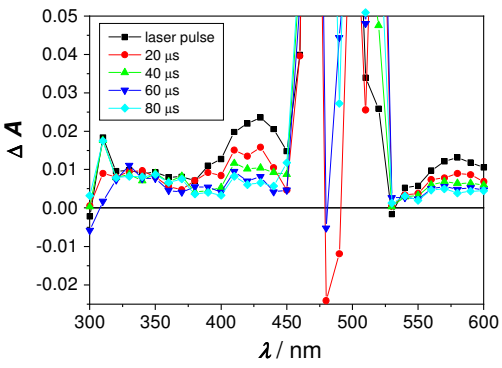


Fig. 2. Transient absorption spectra of **2** in CH_3OH saturated with N_2 after 532 nm laser excitation, $A_{532\,nm} = 0.3$, $E_{532\,nm} = 20$ mJ. Right: the same spectra expanded.

Table 4. Triplet excited state lifetimes (τ_T) for **2** and **3** measured in CH_3OH and CD_3OD.

Compound	τ_T (CH_3OH) / μs [b]	τ_T (CD_3OD) / μs
2	70 ± 10	110 ± 10
3	57 ± 7	150 ± 50

Computational Results

UV/Vis Absorption Spectra

In the TD-DFT computed spectra of **2**, **3**, and **4** (Fig. S21), the S_1 state is well-separated (by ca. 0.7-0.8 eV) from S_2 and the higher-lying singlet states, which is here also supported by the CASSCF/CASPT2 computations (vide infra). The presence of the phenol chromophore at the *meso*-position in **3** and **4** does not alter the spectrum significantly compared to that of compound **2** (Fig. S21). Furthermore, in all three BODIPY compounds, the S_1 band retains the nearly identical position and intensity. To optimally align the experimental and TD-DFT computed spectra, the latter had to be red-shifted by 0.37 eV, which is in line with the previous work on the performance of TD-DFT for a series of BODIPY dyes.[58] This error is also very close to the one reported recently for the CAM-B3LYP functional (0.393 eV) on the example of six BODIPY derivatives.[59] The CASPT2 value for the vertical $S_0 \rightarrow S_1$ transition in **2** is red-shifted by 0.2 eV from the TD-CAM-B3LYP one, and so is by only 0.17 eV off the experimental band peak.

Considering that the S_1 state does not overlap with higher excited states, the clearly visible sub-structure of the strong lowest-lying band peaking at 506 nm, in particular the strong shoulder at 479 nm, must be attributed to the strong vibronic progressions, similarly to what was concluded before for BODIPY dyes.[60] To pinpoint possible reasons behind the observed dual fluorescence, we modelled the vibrationally resolved $S_0 \rightarrow S_1$ band of **2** in the framework of the harmonic Franck-Condon-Herzberg-Teller (FCHT) approximation. Since the S_1 state is central to the studied photolytic reactions, and its NTOs in the **2**, **3**, and **4** are closely comparable (vide infra), we investigated its vibronic structure in more detail (Fig. S22). The most intense region of the $S_0 \rightarrow S_1$ band, in the vicinity of the 505 nm peak, is due to the 0-0 origin and the several near-lying strong vibrational progressions and combinations involving the low-frequency butterfly-twisting motion of the lateral pyrrole rings. The shoulder at 479 nm is primarily due to the symmetric C-C and C-N stretches in the two pyrrole rings coupled to the symmetric H-C-H scissoring of the CH_3 substituents. The remaining discussion on the vibronically most active modes is given in the ESI (Table S2 and the section "Vibrationally resolved spectrum").

It was previously found that the low-lying rotational modes of the *meso*-substituent underpin the strongest vibronic transitions in a BODIPY dye that lacked the CH_3 groups at the C1 and C7 positions.[61,62,63,64] In **2**, however, these groups sterically hinder the rotation of the hydroxymethyl *meso*-substituent. Consequently, in the lower regions of the spectrum, the modes dominated by the butterfly-twisting motion of the BODIPY skeleton become the vibronically most active ones although they give rise to much weaker transitions than does the unhindered rotation of the *meso*-substituents (cf. Fig. S40 from Ref.[65] with Fig. S22). Interestingly, it was shown that the coupling of the *meso*-rotation and butterfly-twisting provides a route to the radiationless de-excitation of the S_1 state in BODIPY dyes with unsaturated *meso*-substituents.[63]

The photoexcitation of **2** at 445 nm in the SPC measurements should significantly populate the higher vibrational levels of the S_1 state, in particular those close to the 0-0 origin (Fig. S22), and so the emission from these levels is likely responsible for the observed multiexponential fluorescence decay. The possibility that fluorescence in solutions could originate from higher vibrational levels of electronically excited states has originally been put forward by Rieckhoff et al.[66]

Potential Energy Surfaces for the Cleavage at Boron

To elucidate the mechanistic details of the photoinduced cleavage of the B-CH_3 bond, we first performed the relaxed scans along the B-C distance on the S_0, S_1 and T_1 surfaces using the DFT (S_0 and T_1) and TD-DFT (S_1) methods. At the obtained geometries, the energies were next re-computed at the multireference CASSCF/CASPT2 level considering several lowest-lying state-averaged singlet and triplet states. The T_1 and S_1 surface scans yielded generally similar geometries, and so in the following we discuss the CASSCF/CASPT2 data obtained at the T_1 and S_0 geometries. Fig. 3 shows the energies of the several lowest CASSCF/CASPT2 states as a function of the B-CH_3 distance.

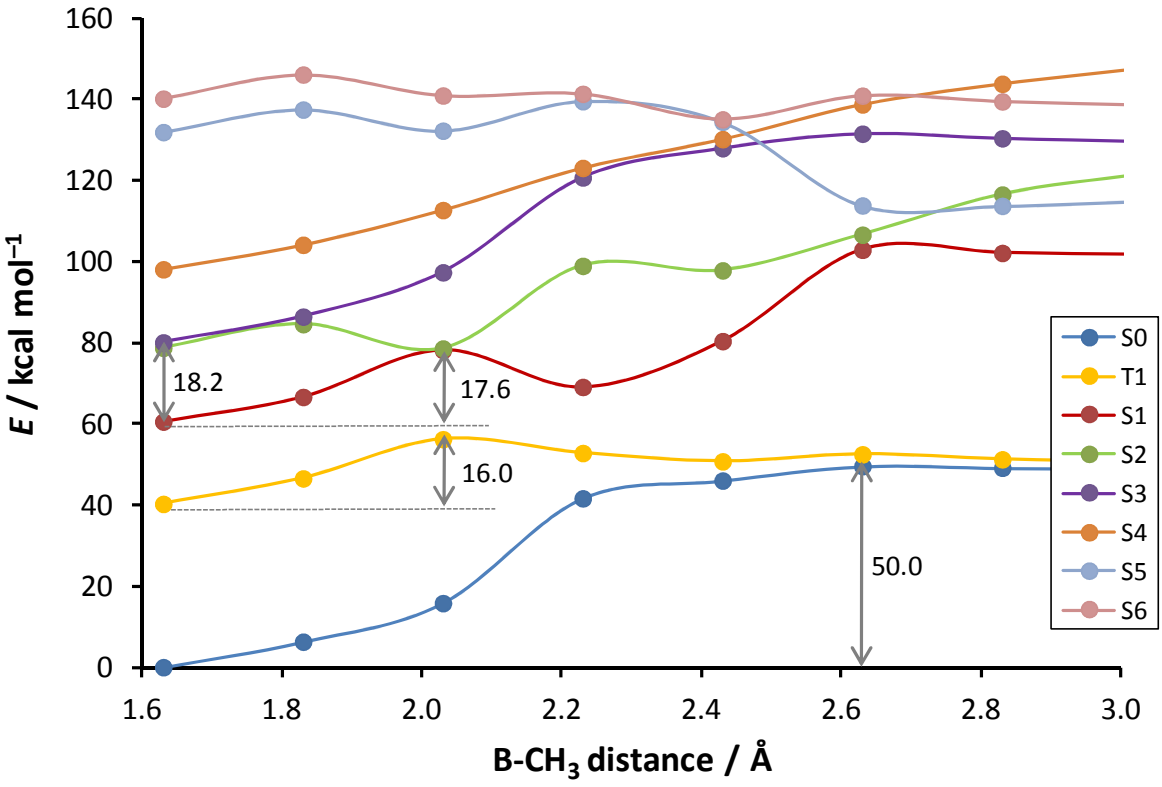
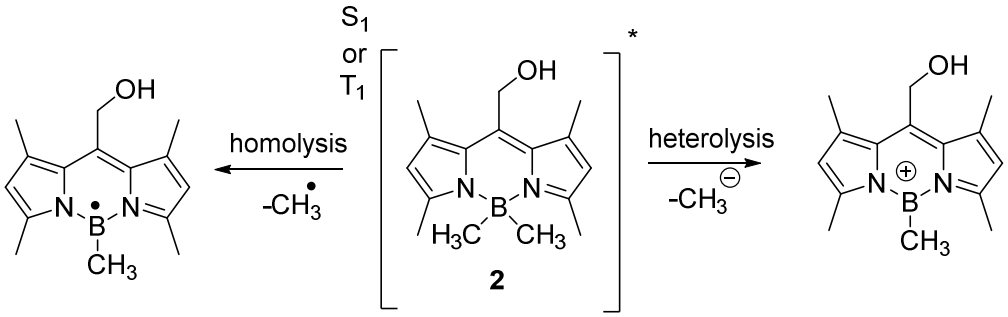


Fig. 3. The CASSCF/CASPT2 single-point energies of the singlet and triplet states of **2** as a function of the B-CH_3 distance. The CH_3OH solvent is described implicitly via the PCM. The geometries are taken from the B3LYP/6-311+G(2d,p) relaxed scan on the T_1 surface. The energy differences are given in kcal mol^{-1}.

Discussion

Mechanism of the Photo-Cleavage at Boron

The cleavage of the C-B bond can in principle be homolytic or heterolytic (Scheme 3). Monitoring changes in the Mulliken atomic charge on the leaving C atom and the molecular dipole moment along the B-CH_3 dissociation curves is useful for characterizing the dissociation of the B-C bond on a given surface. The homolytic dissociation would involve separation into neutral BODIPY• and •CH_3 radicals and thus approximately steady charges and dipole moments. Conversely, the heterolytic dissociation would involve the charge separation resulting in the carbanion $H_3C:^-$ and the positively charged $BODIPY^+$ moiety, formally containing the borenium center. Such a heterolysis would be reflected in the increasing dipole moments and gradual accumulation of the negative charge on the carbon. Table S4 and Fig. S23 demonstrate that the Mulliken charges and dipole moments are consistently correlated throughout the B-CH_3 bond dissociation.



Scheme 3. The homolytic and heterolytic dissociation of the B-CH_3 bond in **2**.

The nature of the dissociation can also be inferred from inspecting the degree of planarization of the CH_3 fragment since the independent $\bullet CH_3$ is D_{3h} planar whereas $H_3C:^-$ is C_{3v} pyramidal. In contrast, when the BODIPY moiety is optimized after the departure of CH_3, it is found that the boron center is fully planar in both $BODIPY^+$ and BODIPY• form (Scheme 3), and that the charges on the B in the two forms are also virtually identical. Thus, the two dissociation mechanisms cannot be distinguished by inspecting the changes in the geometry and charge at the boron center. This is true for the BODIPY moiety in both S_0 and S_1 state, and shows that neither the positive charge nor unpaired spin (Fig. S24) are strictly localized on the boron.

The obtained CASPT2 barriers of 16-18 kcal mol^{-1} in the singlet and triplet excited state manifold may seem relatively high, even for an inefficient photoreaction (Φ_R = 0.021). Such high barriers are primarily attributable to the use of the fully implicit solvation model, and so would likely be reduced in the presence of explicit CH_3OH molecules. Here, it is important to note the earlier work which demonstrated that the electrostatic inductive effects due to the surrounding polarizable continuum alone are generally insufficient to cause a large enough charge polarization and eventual dissociation into the constituting ions. Specifically, it was shown that in order to stabilize the heterolytic dissociation curve below the homolytic one, and thus favor the separation into oppositely charged ions, several explicit molecules of solvent are typically required.[67] Given the size of molecule **2** and the accompanying ambiguities with optimally placing the solvent molecules, performing computation with such a microsolvation is currently unfeasible. We still included one explicit CH_3OH molecule, which was crucial for locating a transition state for the substitution at boron (vide infra). In addition, some of the energy for overcoming the barrier for the C-B dissociation can come from the excess vibrational energy following the photoexcitation.

Since the separation into charged fragments is energetically costly without the support of the explicit solvent, the studied dissociation curves generally exhibit the homolytic limit, i.e. the separation into neutral radicals. A continual increase in the dipole moment along the dissociation curve is not seen before S_5 (Table S4). Interestingly, this is the only state to exhibit an unambiguously heterolytic limit, and, although initially high in energy, later on in the region of 2.8-3.0 Å it even drops below S_2 (Fig. 3). Because such a trend is not seen with the uncorrelated CASSCF curves (Fig. S25), it may be concluded that the inclusion of the dynamic electron correlation via CASPT2 helps support the separation of charge at large C-B distances. Here we also attempted a diabatization of the adiabatic CASSCF curves within the space of the 7 CASSCF roots according to the DQ procedure.[68] However, this did not furnish

additional insights since only the homolytic curves were found to be intermixing owing to their similarly low dipole moments, whereas the heterolytic S_5 state remained largely pure and relatively high in energy.

Focusing on the low-lying states of interest, in the course of the C-B bond elongation, after the initial steady increase, the dipole moment on the S_1 surface falls abruptly by ca. 4 D over the 2.4-2.6 Å region of the C-B distances. Similarly, the drop of almost 5 D is seen between 2.0-2.2 Å on the T_1 surface (Table S4; Fig. S23). We also note at 2.0 Å the conical intersection (CI) between the S_2 and S_1 states, which are initially separated by 18.2 kcal mol^{-1} (Fig. 3). However, this CI is expected to have only a minor bearing on the dynamics of the dissociation because S_2 and S_1 have similarly homolytic cleavage limit.

Focusing on the likelihood of the S_1/T_1 intersystem crossing (ISC), the closest approach of the S_1 and T_1 curves is seen around 2.2. Å at which distance their energy difference lowers to 16 kcal mol^{-1} (0.7 eV). Consequently, around this region the ISC is expected to be the most probable. Note however that initially the S_1 and T_2 states are closer in energy than the S_1 and T_1 suggesting that if the ISC does take place it rather involves the $S_1 \rightarrow T_2$ transition, which is anticipated around the B-C distances of 1.85 Å (Fig. S26), and accounts for the detection of triplets by LFP.

From the comparison of the atomic charges in the S_0 and S_1 state (Table S4), it is seen that the S_1 is capable of supporting the charge separation over a much larger range of C-B distances, more than 2.4 Å, compared to only 2.0 Å on the S_0. Another crucial difference between the S_0 and S_1 dissociation curves is that the latter exhibits a barrier of 17.6 kcal mol^{-1} peaking around 2 Å (Fig. 3). The similar is seen on the T_1 curve with the barrier in this case lowered by 1.6 kcal mol^{-1}. These barrier heights, which effectively correspond to the B-CH_3 bond energy in the S_1 (T_1) state, would be further reduced in real solutions where the heterolysis would be assisted by the CH_3OH solvent. We emphasize that the top of the barrier on S_1 (or T_1) is still within the region characterized by the increasing dipole moments (up to 4.85 D; Table S4) and negative charges on the C atom (up to –0.34 *e*; Table S4), and so still indicative of the separation into $BODIPY^+$ and $H_3C:^-$. After crossing the barrier, a local shallow minimum on the S_1 is encountered around C-B distance of 2.2 Å (Fig. 3). This could correspond to a short-lived $BODIPY^+/H_3C:^-$ contact ion pair which is still sharing a common solvent cage. In the next section we propose that, in order to accomplish the substitution at the boron, it is sufficient that a single CH_3OH molecule interposes between the ions. Such an interposition becomes feasible as the distance between the separating $BODIPY^+$ and $H_3C:^-$ ions approaches ca. 3.5 Å (vide infra). The fully solvated ions are probably never formed.

It is also revealing to compare the CASPT2 energy profiles at the geometries obtained from the T_1 (or S_1) surface scan (Fig. 3) with the CASPT2 profiles obtained at the geometries from the S_0 surface scan (Fig. S27). The differences in these geometries profoundly affect the CASPT2 curves and energetics. Thus, the onset of the barrier with the T_1 (S_1) geometries is much earlier, 2.03 Å, compared to 2.33 Å with the S_0 geometries. Furthermore, the barrier with the T_1 geometries is significantly lower: 17.6 (Fig. 3) vs. 25.8 kcal mol^{-1} (Fig. S27). Thus, the S_1 and T_1 surfaces seem much more attuned to the dissociation of the C-B bond than the ground state.

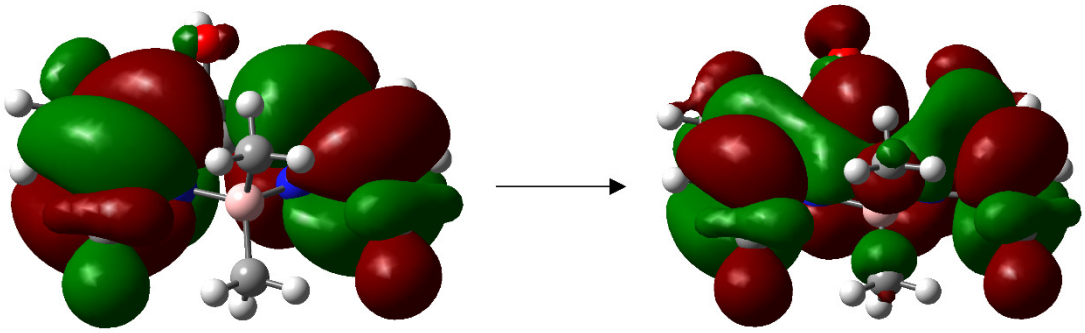


Fig. 4. The natural transition orbitals (hole and particle) corresponding to the S_1 state in **2**. The TD-CAM-B3LYP(+PCM)/6-311+G(2d,p) level of theory is used.

The S_0 potential energy curve resembles a classic Morse-like dissociation with the fragments separated in the asymptotic limit of 50.0 kcal mol^{-1}, which approximates the C-B bond energy in the ground state (Fig. 3). It is thus seen that the photomethanolysis at boron is made possible owing to the C-B bond becoming at least 3 times weaker in the S_1 (T_1) compared to S_0. This can be rationalized by inspecting the natural transition orbitals (NTOs) pertaining to the S_1 transition in **2** (Fig. 4). Thus, in the particle orbital one observes that the σ(B-CH_3) bonds and the π density on the adjacent N atoms are of the opposite phase, which indicates their repulsive interaction, whereas such an interaction is absent in the hole orbital. The analogous observations apply to the S_1 NTOs of **3** and **4** (vide infra). One of the CASSCF active orbitals (Fig. S28; occupation 1.65) likewise points to a similar interaction of the BODIPY core π-system with the bonding σ(B-CH_3) density.

Radical vs. Ionic Mechanism and PCET

Which of the two C-B dissociation mechanisms is more likely to be involved in the photoinduced substitution of the -CH_3 with the -OCH_3 at the boron center, the homolytic or the heterolytic? If the homolysis is operative then the •CH_3 radical intermediate is formed, which would next have to abstract H atom from CH_3OH to form the O-centered CH_3O• radical. Finally, the BODIPY• and CH_3O• radicals would have to recombine to complete the substitution. However, the C-H bonds are more reactive than the O-H bond. Consequently, in the H-abstraction from CH_3OH the C-centered α-hydroxymethyl radical (•CH_2OH) would be predominantly formed.[69] There could also be some ambiguities in the reaction of the CH_3O• and BODIPY• since in the latter the unpaired spin density (i.e. the SOMO) is found to be delocalized over the entire BODIPY π-system (Fig. S24). Finally, the likelihood of the BODIPY• and CH_3O• radicals encountering and colliding in the solution is small and dependent on the diffusion rate. These aspects render the homolysis and the accompanying radical mechanism improbable. Furthermore, the isolated **2-OMe** photoproduct strongly suggests the heterolytic pathway, rather than homolytic.

The heterolysis, on the other hand, involving exclusively the closed-shell charged species seems more likely. In particular, the computations show that the substitution at the boron can be readily carried through via subsequent PCET step taking place on either the S_1 or T_1

surface (Fig. 5). The reaction coordinate of the PCET transition state couples the proton transfer from CH_3OH to $H_3C:^-$ with the transfer of the electron pair from the O atom of the CH_3OH to the boron, which is invested in the formation of the B-OCH_3 bond. Thus, the proton and the electrons are concertedly transferred along the different routes, as is typical of PCET, whereby the photoproduct **2-OMe** and CH_4 (Scheme 4) can be formed in a single step. Note that the formation of CH_4 was also indicated from the irradiation experiments.

As a prelude to the PCET, one molecule of the CH_3OH solvent has to interpose between the borenium center and $H_3C:^-$ whose B and C atoms are 3.47 Å apart. The absolute value of the reaction mode frequency is always larger than 1000 cm^{-1} (see the SI), which is typical of the light particle (i.e. the proton) transfer. In this scenario, the fully solvated and separated ions are probably never formed, which also explains the lack of the detection of the borenium cation in the transient experiments. In the CAM-B3LYP picture, the transition state in the T_1 state is actually closer to the sequential proton transfer-electron transfer given the relatively large O-B distance of 2.8 Å (Fig. 5). Conversely, on the S_1 surface, and also according to B3LYP in both S_1 and T_1 (the coordinates are provided in the SI), the PCET TS can be characterized as rather late because the O-B distance is less than 1.7 Å, and the transferring proton is 0.1 Å closer to the C acceptor than to the O donor.

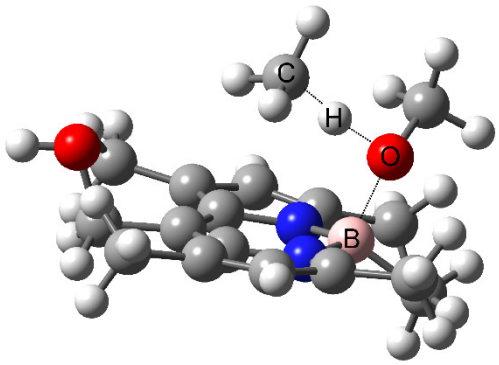


Fig 5. The proton-coupled electron transfer (PCET) transition state in the CH_3OH solution of **2** during the photoinduced cleavage of the B-CH_3 bond. The bond distances computed at the (TD-)CAM-B3LYP-D3(+PCM)/6-311G(d,p) level between the labelled atoms equal: *d*(C-H) = 1.24 (1.27 Å), *d*(O-H) = 1.34 (1.23 Å), and *d*(O-B) = 1.62 (2.80 Å) on the S_1 (T_1) surface.

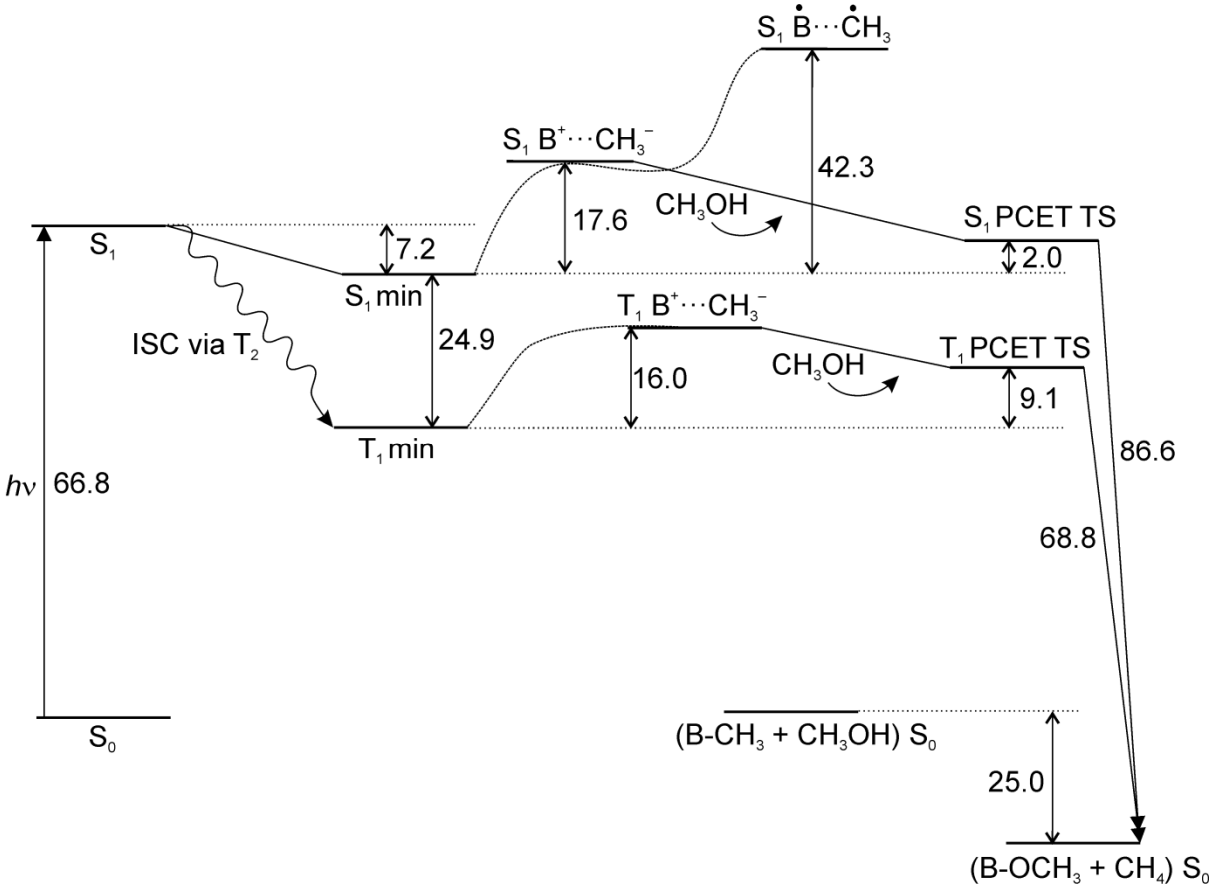
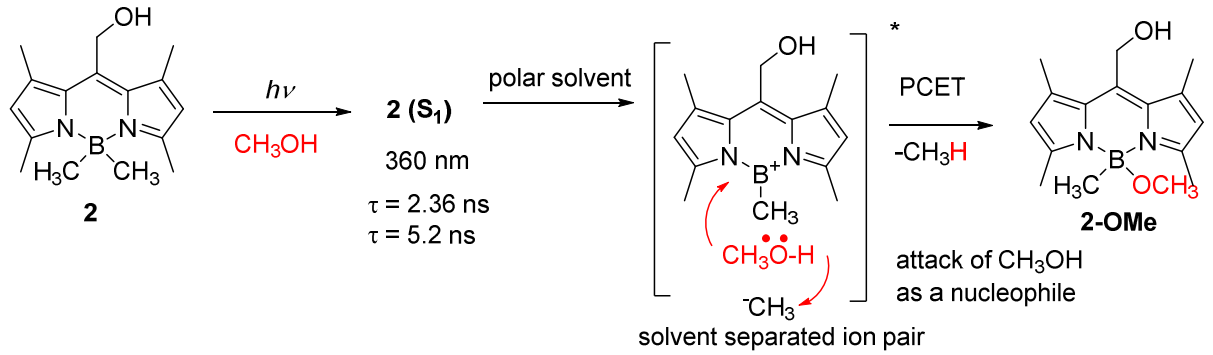


Fig 6. Potential energy profile (kcal mol^{-1}) for the photo-substitution at boron in **2** computed using the (TD-)CAM-B3LYP(+PCM)/6-311G(d,p) method. The S_1 and T_1 C-B bond dissociation energies are taken from the CASPT2(+PCM)/cc-pVDZ level (Fig. 3).



Scheme 4. Photomethanolysis mechanism on boron atom in **2**.

The computed energy for the photoreaction **2** + CH_3OH → **2-OMe** + CH_4 equals –25 kcal mol^{-1} (Fig. 6, **2** and **2-OMe** in the ground state). Since this is an exoergic process and the PCET TS is late with the B-O bond practically formed, its energy on the S_1 (or T_1) surface is relatively low (Fig. 6). Consequently, the PCET is predicted to be very rapid and a sizeable H/D PKIE on account of this step is not expected. This is in line with the experimental data which point to only a modest H/D PKIE for the reactions from the singlet excited state when the reaction is conducted in the CD_3OD solution. We thus conclude that the preceding much

slower heterolysis of the C-B bond should be the dynamical bottleneck and the rate-determining step for the photomethanolysis at boron in **2**. For the reactions taking place from the triplet excited state, the C-B bond dissociation energy is lower indicating a larger KIE, which was indeed observed by LFP.

It is reasonable to assume that, once the photoinduced separation into $BODIPY^+$ and $H_3C:^-$ is under way, the nascent carbanion can rapidly react with any nearby CH_3OH molecule and the same is valid for the borenium center. The latter in particular tends to planarity during the heterolysis, and so CH_3OH could also continually approach from the side opposite to the leaving carbanion in an S_N2-like fashion. Since the PCET and S_N2-like substitution differ with respect to the CH_3OH approach to the boron, the two mechanisms could bring about different stereochemistry in BODIPY dyes with the chiral boron center.

While strictly taking the above PCET route might not be dynamically necessary, the found PCET TS at least shows that it is possible to have a very rapid concerted reaction when $H_3C:^-$ and borenium center are still relatively close and requiring the interposition of only one CH_3OH molecule. This simplicity stands in contrast to the hydrogen atom transfer (HAT) from CH_3OH to $\bullet CH_3$, which would be operative in case of the homolytic radical mechanism, and for which it is difficult to envisage how it could be concerted to the formation of the B-OCH_3 bond.

We finally comment on the adiabaticity of the photomethanolysis at boron in **2**. In the geometry of the PCET TS in the S_1 state, the energy separation between the S_1 and S_0 state is 1.3 eV while the PCET TS on the T_1 surface is 1.2 eV above the S_0. Following the S_1 dissociation curve (Fig. 3), we find no evidence for the CI between the S_1 and S_0 surfaces; the two surfaces draw at their closest at 2.2 Å, at which point their energy difference is still more than 1 eV. Thus, the dissociation curves indicate that the B-CH_3 bond scission proceeds fully adiabatically with the reaction taking place on the S_1 surface throughout. The adiabaticity of the photomethanolysis at boron is also in line with the subsequent PCET step for which the transition state can be located only on the S_1 and T_1 surface but not in the ground state, and with the fs-TA measurements where no intermediate was detected. We reiterate, however, that in the region of the abrupt changes in the dipole moments, ipso facto the changes in the nature of the CASSCF reference, the implicit solvent becomes insufficient for the description of the dissociation. It is precisely in this less reliable region that the S_1 curve starts rapidly ascending and diverging away from the S_0 (Fig. 3). Thus, the S_1/S_0 CI could possibly occur if the heterolytic nature of the S_1 dissociation curve were to be continued beyond 2.4 Å. In such a scenario, the borenium cation would be formed in the ground state (S_0), followed by an attack of CH_3OH in the typical S_N1 like fashion.

In light of the proposed mechanism, we can offer a tentative explanation why in **3** the photomethanolysis at boron is more efficient than in **2** (ca. 2.4 times; vide supra Table 1). We first note a small difference in the C-B bond length in the S_1 state, viz. in **3** this bond is longer by 0.015 Å, and therefore, to a certain extent weaker than in **2**. One can next evoke in **3** a larger participation of the reaction in the T_1 state (Table 1), which is expected to be faster than the reaction on the S_1 surface owing to the smaller barrier for the dissociation of the C-B bond (vide supra). Finally, although the *meso*-substituent in **3** is much bulkier than in **2**, its minimum conformation does not pose any appreciable steric hindrances to the departure of

$H_3C:^-$ and the approach of CH_3OH. This is unlike the situation with the reactant **4** (vide infra).

Mechanism of the Photo-cleavage of the *meso*-Substituent

Whereas the irradiation of **2** and **3** predominantly leads to the substitution at the boron, in **4** the photo-cleavage of the *meso*-substituent followed by elimination of the phenyl moiety becomes the preferred reaction route (Scheme 1). We attempt to elucidate the underlying photochemistry mainly by scrutinizing the relevant bond dissociation curves. Because sensible active spaces in **3** and **4** would grow unfeasibly large, the photo-cleavage of the phenyl substituents was studied using solely (TD-)DFT. This creates additional difficulties because (TD-)DFT dissociation curves, and hence derived bond strengths, are often of uncertain reliability owing to the self-interaction error (SIE).[70] The herein used CAM-B3LYP is the long-range corrected hybrid functional, which is beneficial for reducing the SIE, and has showed a good performance in the recent study on the influence of the SIE on various dissociation processes.[71]

As noted above, the UV/Vis spectra of **2**, **3** and **4** are qualitatively similar (Figs. S3, S5, S7), which is also confirmed by the TD-DFT computations (Fig. S21). The similarities include the dominant S_1 band centered just above 500 nm, which exhibits a rich vibronic sub-structure and is well-separated from the higher-lying bands. Likewise, in all three compounds the next lowest state, S_2, is of the much lower intensity and centered on the verge of the UV region, just below 400 nm (Figs. S3, S5, S7, and S21). Overall, in analogy to **2**, we assume that, under the conditions of exposure to the visible light, the photochemical reactions of **3** and **4** are initiated practically exclusively from the S_1 state.

Properties of the Ether Bonds in 3 and 4 and their Photo-cleavage

We begin by analyzing the properties of the two ether bonds of the *meso*-substituent, designated by C_{Ph}-O (C_{Ph} ≡ phenyl C atom) and C_M-O (C_M ≡ methylene C atom), which are anticipated to undergo the photo-cleavage. The particle NTOs in the S_1 state of **3** and **4** (Fig. 7) are significantly delocalized over the ether bonds, and include the $\sigma(C_{Ph}\text{-}O)$ bonding interaction and the nodal plane intersecting the C_M-O bond. Accordingly, in the S_1 minima of **3** (**4**), the C_M-O bond is slightly extended by 0.015 (0.018 Å), whereas the C_{Ph}-O bond is slightly shortened by 0.003 (0.003 Å) relative to their lengths in the S_0. Both ether bonds are slightly longer in **4** compared to **3**, viz. by 0.016 (0.019 Å) for C_M-O and by 0.007 (0.007 Å) for C_{Ph}-O in the S_0 (S_1) state. Based on the NBO charges, the C_{Ph}-O bond is significantly more polarized than C_M-O; in the S_0 minima of **3** (**4**), the absolute charge differences, $|O - C_{Ph}|$ and $|O - C_M|$, equal 0.89 (0.86*e*) and 0.51 (0.54*e*), respectively. The strong polarization of the C_{Ph}-O bond, which is further increased in S_1, already anticipates the heterolytic nature of the C_{Ph}-O photodissociation.

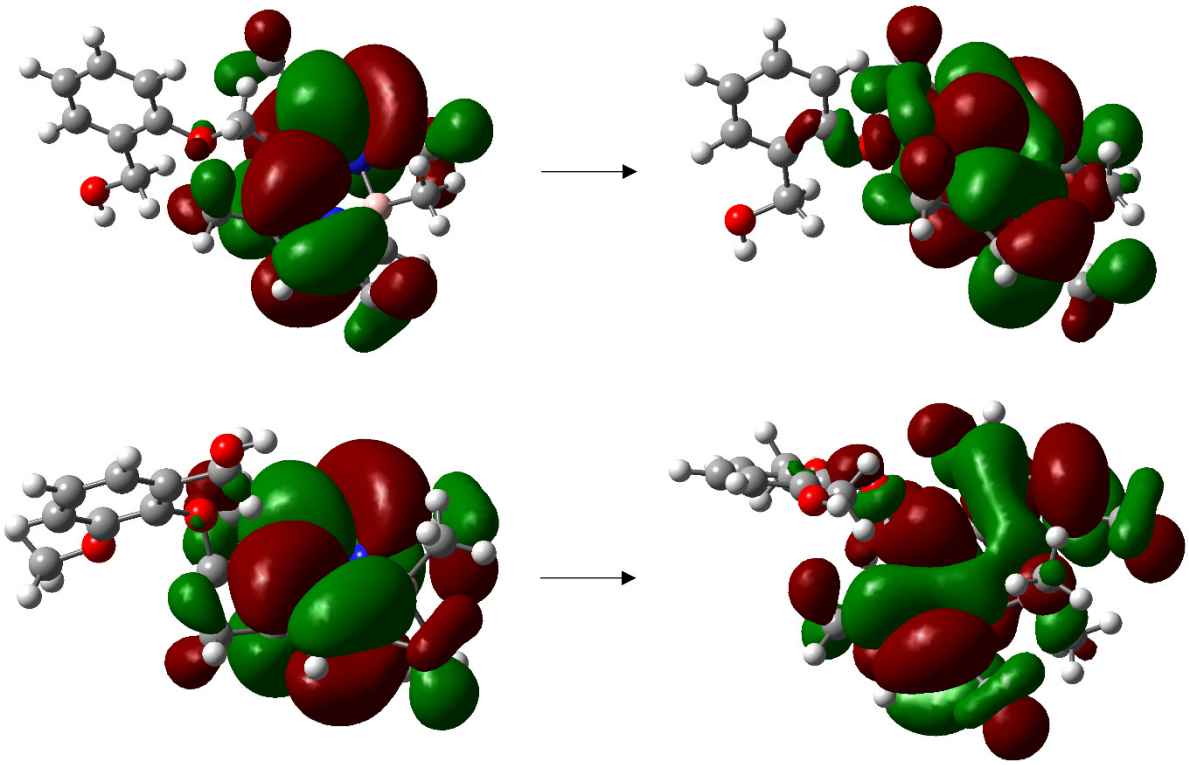
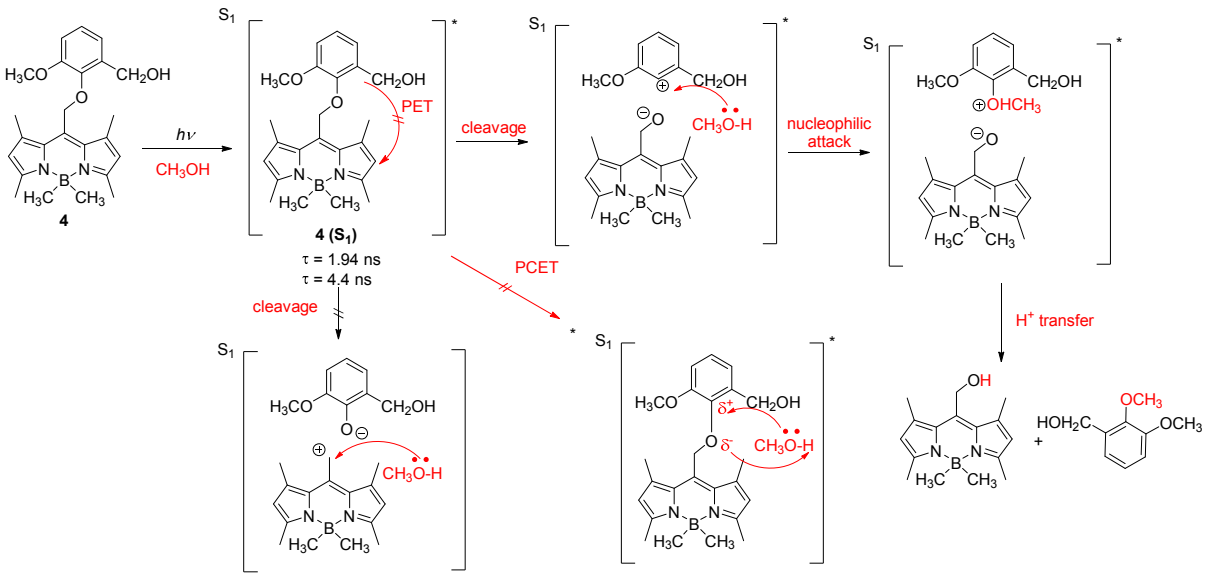


Fig. 7. The NTO orbitals (hole and particle) corresponding to the S_1 state in **3** (above) and **4** (below). The TD-CAM-B3LYP(+PCM)/6-311+G(2d,p) level of theory is used.

The strengths of the two ether bonds in the S_0 state of **3** (**4**) estimated from the Morse fits of the dissociation curves (Fig. S29) equal 141 (142 kcal mol^{-1}) for the C_{Ph}-O and 79 (75 kcal mol^{-1}) for the C_M-O bond. In the S_1 state, these bond strengths were estimated from the highest points on the S_1 curves, which are typically at the top of the small barriers preceding the S_1/S_0 CI. Compared to the S_0 curves, on the S_1, the energy plateau is reached at significantly smaller C-O distances, i.e. the S_0 potentials are typically much wider. The ether bonds are found to be ca. 2 to 5 times weaker in the S_1 compared to the S_0; namely, 72 (67 kcal mol^{-1}) for the C_{Ph}-O and 20 (14 kcal mol^{-1}) for the C_M-O bond in **3** (**4**). Their weakening upon the photoexcitation to the S_1 can be anticipated from the particle NTOs (Fig. 7) where one observes their strong mixing with the π^* virtual levels of the BODIPY core (cf. also the particle NTO in the S_1 state of **2**; Fig. 4). The presence of the -OCH_3 phenyl substituent in **4** slightly weakens the ether bonds relative to **3**, and the effect becomes more pronounced in the S_1 state.

The above computations reveal that in both S_0 and S_1 states of **3** and **4**, the C_M-O bond is several times weaker than the C_{Ph}-O bond. Surprisingly, however, it was observed that the irradiation of **4** results in the photoproduct with the -CH_2OH group at the *meso*-position, which is consistent with the cleavage of the much stronger C_{Ph}-O bond (Scheme 5).



Scheme 5. Photomethanolysis mechanism at the *meso*-position in **4**.

In the following, we present computational evidence that the photo-cleavage of the C_M-O bond, which in methanol would lead to the photoproduct having the -CH_2OCH_3 substituent at the *meso*-position, cannot run to completion on the S_1 surface. This stands in sharp contrast to the photo-cleavage of the C_{Ph}-O bond leading to the -CH_2OH substituent at the *meso*-position, which, despite requiring more activation energy, is photochemically allowed and indeed adiabatic on the S_1 surface.

We investigated how C_{Ph}-O and C_M-O dissociation curves in the S_1 state of **4** are affected by the presence of one explicit molecule of the CH_3OH solvent (Figs. 8 and S30). The optimum placing of the explicit CH_3OH is such that it forms hydrogen bond with the ether O atom as the acceptor. Focusing on the C_{Ph}-O bond, its bond energy is reduced from 67 to 63 kcal mol^{-1}, and the hydrogen (O···H) bond distance shortens considerably from 1.9 to 1.6 Å in the course of the dissociation (Fig. 8). In the final stages of the C_{Ph}-O dissociation, another strong H-bond is formed between the accepting ether O atom and the -CH_2OH substituent on the phenyl ring as the donor. Conversely, in the course of the C_M-O bond dissociation, the H-bond distance is shortened only slightly, and the C_M-O bond energy is practically unaffected by the presence of CH_3OH. Near the end of the C_{Ph}-O and C_M-O dissociation curves, the |O - C_{Ph}| and |O - C_M| differences in the NBO charges amount to 0.89 and 0.58*e*, respectively.

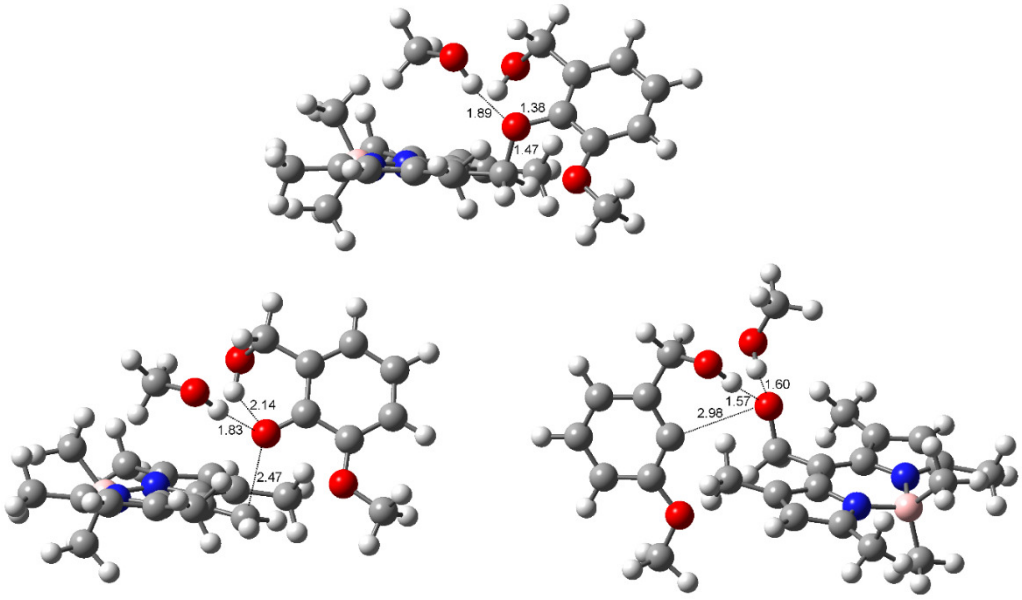


Fig. 8. The initial structure of **4** + CH_3OH (top) and the approximate structures of the conical intersections (below) in the course of dissociation of C_M-O (left) and C_{Ph}-O (right) bonds. The C-O and hydrogen bond distances (in Å) are indicated. The S_1–S_0 energy differences at the approximate CI geometries equal 0.08 (C_M-O) and 0.03 eV (C_{Ph}-O). The (TD-)CAM-B3LYP(+PCM)/6-311G(d,p) level is used.

The presence of already one explicit molecule of CH_3OH tangibly softens the C_{Ph}-O bond, and brings about the formation of the strong H-bonds with the ether O atom in the role of the H-bond acceptor. Furthermore, the polarization of the dissociating C_{Ph}-O bond is uniformly strong throughout, and is significantly larger than the polarization of the C_M-O bond. These occurrences clearly uphold the heterolytic nature of the C_{Ph}-O dissociation which thus gives rise to the negatively charged alkoxy moiety and the phenyl carbocation (Scheme 5).

It is also illuminating to compare the C_{Ph}-O and C_M-O bond dissociation energies estimated from the Morse fits (Table S5; Fig. S29) with the reaction energies for the dissociation into the (infinitely separated) radicals (i.e. the homolysis) or ions (i.e. the heterolysis). While we were only able to produce these data for the S_0 state, roughly similar observations are expected to apply to the S_1 surface. In case of both C_{Ph}-O and C_M-O dissociation, the value of the reaction energy for creating the ion pair is very close to the bond dissociation energy from the Morse fit (Table S5). This happens even though the radical pair is predicted as more stable than the ion pair, which is attributable to the deficiencies in the description of solvated ionic species within the implicit solvent framework. Interestingly, following the heterolytic dissociation of one of the ether bonds in **4**, the ground state of the resulting carbocations is predicted as triplet. Thus, the C_{Ph}- and C_M-centred triplet carbocations are respectively by 4 and 25 kcal mol^{-1} more stable than their singlet counterparts. Conversely, the C_{Ph}-centred singlet carbocation of **2** is by 16 kcal mol^{-1} more stable than the triplet. The electronic configurations of carbocations in the ground state have been investigated.[72]

The crucial difference between the C_{Ph}-O and C_M-O dissociation on the S_1 is in the C-O distances at which the S_1/S_0 CI is encountered. In **4**, this critical distance is around 2.7 Å for

the C_{Ph}-O and 2.1 Å for the C_M-O curve. Around this region, the S_1 and S_0 state become very close in energy and the scan typically terminates because of the non-converged SCF step. The explicit CH_3OH molecule (Fig. 8) delays the onset of the S_1/S_0 CI for both bonds to 2.9 Å for C_{Ph}-O and 2.4 Å for C_M-O (Figs. S28 and S29). The onset of the S_1/S_0 CI along the dissociation curve is important because the earlier it is, the less chance there is for a successful completion of the photo-cleavage and the subsequent substitution. The reason is that, upon return to the S_0 surface, the C-O bond will reform rapidly if the C-O distance is too small and the energy of the dissociating fragments too low to overcome the much deeper and wider S_0 potential (Fig. S29). Thus, the longer the C-O bond dissociates along the energetically less steep S_1 potential, the larger the distance between the dissociating fragments, and consequently the easier it is for the molecule of the CH_3OH solvent to interpose between them and finalize the substitution at the O center (see the discussion on the photoproducts below). It can be concluded that the too early S_1/S_0 CI is likely the key reason why the dissociation of the C_M-O bond, despite its relatively small bond energy, remains largely inefficient upon the photoexcitation to the S_1 state.

To further rationalize why in **4** the observed *meso*-substitution product originates from the photo-cleavage of the C_{Ph}-O but not the C_M-O bond, we next investigate how these products could have been formed on the S_1 surface. For a detailed discussion see the SI (Figs S31-S34, and the section entitled Reactivity of the Substitution Photoproducts). In summary, we were able to prove computationally that the anticipated photoproduct from the C_M-O bond cleavage could not have been formed on the S_1 surface, whereas the one from the C_{Ph}-O bond cleavage could.

We additionally consider a possibility of photo-cleavage mechanism in **4** involving photoinduced electron transfer (PET) from the phenol part of the molecule to the BODIPY, followed by heterolysis (see Scheme S2, Table S6 and Figs S35 and S36). If operative, it would account for the photo-cleavage of the C_{Ph}-O bond distant from the BODIPY chromophore and circumvent large energy barriers for the homolytic or heterolytic cleavage. Since **4** formally consists of the two disjoint chromophores, viz. the phenyl ring (Phe) of the *meso*-substituent and the BODIPY π-system, the PET process can be modeled in analogy to our previous studies on the BODIPY pH sensor[65] and the quinazoline drug doxazosin.[80] However, comparison of the electron affinity for the excited BODIPY and ionization potential for the phenyl indicates that the PET is not feasible (for details see the SI). Moreover, similar values for Φ_F (Table 2) for **3** and **4** are also not in agreement with the PET deactivation pathway from **4** (S_1). We also reiterate that the NTOs of the S_1 state (Fig. 7) indicate that the excitation of the BODIPY core also affects the strength and reactivity of the ether bonds of the *meso*-substituent (vide supra); thus, a process such as PET is not necessary to trigger the elimination at the *meso*-position. Consequently, the most likely photo-cleavage mechanism in **4** involves the heterolysis of the C_{Ph}-O bond taking place predominantly from the singlet state; nonetheless, the residual less efficient triplet state reactivity is also possible.

Competition Between the *meso*- and the Substitution at Boron

Compared against the CASSCF/CASPT2 B-CH_3 bond energy (vide supra), the relatively large C_{Ph}-O bond energy obtained from the CAM-B3LYP dissociation curves would suggest that, in this class of BODIPY dyes, the photoinduced *meso*-substitution could not be

competitive to the substitution at boron. However, as discussed above, the reliability of both results could to a varying degree suffer from the inadequacy of the purely implicit solvent model to provide a balanced description of heterolysis vs. homolysis. The (TD-)DFT results may additionally be in error due to the difficult-to-correct spurious self-interaction of the electron density, termed the SIE. The full discussion of the SIE and its possible effects on the accuracy of the herein computed (TD-)DFT dissociation curves is given in the SI (section entitled Effects of the Self-Interaction Error (SIE) and Figs. S32 and S37).

Finally, we hint at possible reasons why in **4**, unlike in **3**, the *meso*-substitution becomes preferred over the substitution at the boron. The above results indicate that the extra -OCH_3 substituent on the phenyl ring in **4** weakens the C_{Ph}-O bond by ca. 5 kcal mol^{-1}. As to the structural differences between **3** and **4**, the most conspicuous one is the preferred conformation assumed by the *meso*-substituent (Fig. S38). In **3**, the *meso*-phenyl ring is exactly perpendicular to the BODIPY plane whereas in **4** the unfavorable steric clash between the phenyl -OCH_3 and -CH_2O- at the *meso*-position force the phenyl ring to tilt considerably; the relevant C-O-C-C dihedral angle equals 180° in **3** and 114° in **4** (Fig. S38). This structural difference could impede the departure of $H_3C:^-$ after the B-CH_3 cleavage because of the steric hindrance imposed by the -OCH_3 group which now partly protrudes above the BODIPY rings. To verify this, for **3** and **4** we optimized the PCET transition states for the substitution at the boron (see the SI for the TS structures), analogous to the one discussed in case of **2** (vide supra). The stronger steric strains in the PCET TS of **4** are revealed by the non-covalent interaction (NCI) plot (Fig. S39). Relative to the corresponding reactants, these strains make the PCET transition state of **4** less stable by 2.4 kcal mol^{-1} compared to that of **3**.

Conclusion

Combined theoretical and experimental investigations described herein fully unraveled the mechanistic details of the photo-cleavage of the important class of BODIPY photocages at the boron and at the *meso*-methyl position. BODIPY compounds bearing a phenoxyl (poor leaving group) at the *meso*-methyl substituent, undergo the photo-cleavage at the boron atom. The heterolytic cleavage yields a tight borenium cation and methyl anion, that can be intercepted with CH_3OH and undergo proton-coupled electron transfer to produce methane and borenium ether photoproduct. The introduction of a methoxy group to the phenoxyl leaving group redirects the reaction at the boron to the cleavage of the ether. The ether photo-cleavage regiochemistry (the phenyl-O vs. alkyl-O bond) is primarily determined by the position of the CI between the S_0 and S_1 states. The alkyl-O bond cleavage is prohibited in the S_1 due to a CI reached after a short elongation of the C-O bond, resulting in a nonproductive pathway and the deactivation to S_0. On the other hand, albeit stronger, phenyl-O bond does cleave on the S_1 surface since it can be elongated significantly more than the alkyl-O bond before it reaches the non-productive CI. The elucidation of all mechanistic details for the photo-cleavage reactions are important for the rational design of new BODIPY photocages that can be cleaved on boron. Furthermore, for the ultimate application of BODIPY photocages in biology it is important to know all intermediates en route since they may interfere with biological targets.

Experimental and Computational Methods

Compounds **2**-**4** were prepared according to previously described procedure.[46]

Irradiation of 2 in Methanol

BODIPY **2** (30 mg, 0.11 mmol) was dissolved in CH_3OH (30 mL, $c = 3.7 \times 10^{-3}$ M). The solution was poured in two quartz test tubes, sealed with a rubber septum and purged with a stream of N_2 for 20 min. The solution was irradiated in a Luzchem reactor with 8 cool white lamps (wavelengths 400-700 nm) over 36 h.[73] The test tubes were placed in the middle of the reactor, equally separated from the lamps (15 cm from each side). The reactor was cooled by a fan. After the irradiation, the composition of the solution was analyzed by HPLC indicating 80% conversion (for the HPLC method see the SI). The solvent was removed on a rotary evaporator and the residue was chromatographed on a column of aluminum oxide (activity IV, 10% H_2O) using CH_2Cl_2/EtOAc (20%) as eluent to afford 12 mg (38%) of photoproduct **1-OMe** in the form of red crystals.

(5-Methoxy-1,3,5,7,9-pentamethyl-5H-4λ^4,5λ^4-dipyrrolo[1,2-*c*:2',1'-*f*][1,3,2]diazaborinin-10-yl)methanol (**2-OMe**) mp > 250 °C decomp.; ^{1}H NMR (600 MHz, $CDCl_3$): δ 6.08 (s, 2H), 4.93 (s, 2H), 2.93 (s, 3H), 2.52 (s, 6H), 2.50 (s, 6H), 0.01 (s, 3H), the OH signal was not observed; ^{13}C {^{1}H} NMR (150 MHz, APT, $CDCl_3$): δ 154.8 (s), 138.7 (s), 138.2 (s), 132.0 (s), 122.1 (d), 56.3 (t), 49.0 (q), 15.8 (q), 15.0 (q), 0.0 (q). HRMS (ESI, Q-TOF), *m/z*: [M-OCH_3]$^+$ calculated for $C_{15}H_{19}BN_2O^+$ 254.1699, found 254.1703.

Caution! CH_2Cl_2 is a carcinogenic substance and it causes skin and eye irritation, and CH_3OH is a toxic substance. A care should be taken when handling these substances, which should be done in a fume hood. Protective eyewear and gloves should be worn.

Absorption and Fluorescence Measurements

Absorption spectra were recorded on a PG T80/T80+ spectrophotometer at rt. Fluorescence measurements were performed on an Edinburgh FS5 fluorometer by use of slits corresponding to the bandpass of 1 nm for the excitation and the emission. The samples were dissolved in CH_3CN, CH_3OH or CD_3OD (1:1, phosphate buffer pH 7.0, 50 mM) and the concentrations were adjusted to absorbances of less than 0.1 at the excitation wavelengths of. Fluorescence quantum yields were determined by use of rhodamine B in CH_3OH as a reference ($\Phi_F = 0.66$).[56] One fluorescence measurement was performed by exciting sample at three different wavelengths and the average value was calculated (Eq. S1). Prior to the measurements, the solutions were purged with Ar for 20 min. The measurement was performed at rt (25 °C).

Time-correlated single photon counting (TC-SPC) measurements were performed on an Edinburgh Instruments FS5 spectrometer equipped with a pulsed LED at 445 nm (the pulse duration ≈ 800 ps). Fluorescence signals at 550 nm were monitored over 1023 channels with the time increment of ≈ 20 ps/channel. The decays were collected until they reached 3000 counts in the peak channel. To obtain the instrument response function (IRF), a suspension of silica gel in H_2O was used as a scattering solution. Prior to the measurements the solutions were purged with a stream of N_2 for 20 min. The measurement was performed at rt (25 °C). Decays of fluorescence were fit to a sum of exponentials according to Eq. S2 in the SI.

Caution! CH_3CN is a toxic substance and it causes skin and eye irritation. A care should be taken when handling the substance, which should be done in a fume hood. Protective eyewear and gloves should be worn.

Laser Flash Photolysis

The LFP measurements were performed on a LP980 Edinburgh Instruments spectrophotometer equipped with a Q-smart Q450 Quantel YAG laser, frequency doubled at 532 nm. The energy of the laser pulse at 532 nm was set to 6 or 20 mJ and the pulse duration was 7 ns. Absorbances at the excitation wavelength were set to 0.3. The solutions were purged for 15 min with Ar or O_2 prior to the measurements, which were conducted at 25 °C.

Caution! High power laser irradiation is damaging to biological tissues. Caution is required when working with the lasers and protective eyewear must be used at all times.

fs-TA Spectroscopy

For the excitation Light Conversion Orpheus–Vis optical parametric amplifier (OPA) delivering 50 fs pulses at 500 nm was used. The OPA was pumped using Light Conversion Pharos femtosecond Ytterbium DPSSL system from which a small part of the output beam was used for the supercontinuum generation in CaF_2 plate that served as a broadband probe beam covering 340-700 nm wavelength range. A homemade transient absorption spectrometer was built around a Hamamatsu S7030−1006 detector equipped with read-out electronics capable of single-shot measurement of the probe spectrum at the 1 kHz laser repetition rate (Entwicklungsbuero EB Stresing, Berlin, Germany). Both beams were focused onto a 0.5 mm path length quartz flow cell (48/UTWA2; Starna) connected to the pumping system in which unidirectional non-recirculating flow was used. In addition to selecting appropriate flow speed, unidirectional non-recirculating flow ensured that each pulse excites fresh sample in order to exclude the possibility of exciting photoproducts. This scheme somewhat limited the signal to noise ratio of our measurements as the duration of the experiment was limited by the amount of available solution (500 mL).

Computational Methods

The mechanisms of the photo-substitution at the boron and *meso*-position in **2**, **3**, **4** were investigated using (time-dependent) density functional theory (TD-DFT), the multiconfigurational complete active space self-consistent field (CASSCF) method,[74] and the multireference second-order perturbation theory based on the CASSCF reference wave functions (CASPT2).[75]

For the exchange-correlation (XC) density functionals we chose the standard hybrid B3LYP (using formula III from the VWN study)[76,77,78] and its range-corrected variant CAM-B3LYP.[79] These XC functionals have repeatedly been shown to predict reasonable absorption spectra,[65,80] reaction mechanisms and energetics,[81] and bond dissociation curves.[82] The DFT "ultrafine" pruned integration grid consisting of 99 radial shells and 590 angular points per shell was used. The CH_3OH and CH_3CN solvents were described implicitly using the polarizable continuum model (PCM)[83] in conjunction with the integral equation formalism

(IEFPCM).[84] The solute cavities were constructed from the overlapping atom-centred spheres of the United Force Field (UFF) radii scaled by the factor of 1.1, with H atoms having their individual spheres. The integration over the cavity surface was performed using the Lebedev–Laikov quadrature of approximately 5 points/Å^2 density. The dielectric constants of methanol and acetonitrile equal 32.613 and 35.688, respectively. The electronic DFT energies of the solute are corrected for the dispersion interactions according to the empirical D3 parametrization tailored to the B3LYP and CAM-B3LYP functionals.[85] The use of the PCM is henceforth emphasized by inserting the (+PCM) designation next to the computational method.

The dissociation of the B-CH_3 bond in **2** was studied using the multireference CASSCF/CASPT2 treatment[74,75] with the Dunning's double-ζ cc-pVDZ basis set.[86] First, the relaxed scans along the B-CH_3 distance were carried out at the B3LYP(+PCM)/6-311+G(2d,p) level on the S_0 and T_1 surfaces and at the TD-CAM-B3LYP(+PCM)/6-311G(d,p) level on the S_1 surface. The T_1 surface scan was performed by setting the triplet multiplicity and adopting the spin-unrestricted B3LYP method while for scanning the S_1 surface we used the space of the 4 lowest TD-DFT roots. Next, at the geometries obtained from these scans, we computed the CASPT2 single-point energies, and CASSCF dipole moments and Mulliken partial atomic charges using the CASSCF reference wave function built from 12 electrons in 11 active orbitals resulting in 60984 configuration state functions. The (12,11) active space includes the 11 occupied and virtual orbitals of the BODIPY core π-system, and was previously shown to be sufficient for a reliable description of the low-lying excited states in the series of BODIPY dyes.[58] The pseudonatural active orbitals and their approximate occupancies are shown in Fig. S28. The state-averaged CASSCF formalism was used with averaging performed over 7 equally weighted lowest roots. The CASPT2 computations were performed as single-state, and the standard value of the IPEA level shift of 0.25 au was used.[87] Additionally, to mitigate the problems with intruder states and the too low reference weights, imaginary level shift[88] of 0.1 au was applied. In all the multireference computations, the solvent was described implicitly by adopting the conductor version of the PCM,[89] which is known to be a good approximation for polar solvents such as methanol. The average area of the solute cavity tesserae was 0.2 Å^2. To ensure the convergence of the CASSCF(+PCM) equations, the minimum radius of the spheres used to smooth out the cavity surface had to be increased to 1.5 Å.

In **3** and **4** the additional phenolic π-chromophore at the *meso*-position considerably enlarges the minimum sensible active space, thus rendering the multireference methods unfeasible. Therefore, the dissociation curves corresponding to the phenyl-O (C_{Ph}-O) and alkyl-O bonds (C_M-O) in the S_0, S_1, and T_1 states of **3** and **4** were studied using solely the (time-dependent) DFT at the (TD-)CAM-B3LYP-D3(+PCM)/6-311G(d,p) level.

Finally, the energies and intensities of the vibronic $S_0 \rightarrow S_1$ transitions in **2** were computed in the framework of the harmonic Franck-Condon-Herzberg-Teller (FCHT) approximation using the full Duschinsky transformation.[90] To this end, the minima of the S_0 and S_1 states and the corresponding (unscaled) harmonic vibrational frequencies were computed at the same level, viz. (TD)-CAM-B3LYP-D3(+PCM)/6-311+G(2d,p). The maximum quantum number considered for the individual modes and for the combination bands were set to 30 and 20, respectively. The vibrationally resolved spectra were convoluted using Gaussian line shapes with half-width-at-half-maximum (HWHM) parameters of 30 and 400 cm^{-1} (Fig S22).

The Gaussian 16[91] (DFT(+PCM) and TD-DFT(+PCM)) and OpenMolcas 22.06[92] (the multireference computations) quantum chemistry codes were used. The noncovalent interactions were analyzed and plotted (Fig. S36) by means of the NCIPLOT-4.2 program.[93]

ASSOCIATED CONTENT:

• ***Data Availability Statement***

The data underlying this study are available in the published article, in its Supporting Information , and openly available in and openly available in Public Documents_HrZZ-IP-2019-04-8008 at: https://mojoblak.irb.hr/s/PXPWDXZ2QCp3daC.

• ***Supporting Information Statement***

Supporting information contains detailed experimental procedures for the photochemistry, determination of the photoreaction quantum yields, UV-vis and fluorescence data, fs-TA and LFP data, computational details, copies of ^{1}H and ^{13}C NMR spectra and coordinates of the optimized molecular structures. The Supporting Information is available free of charge on the website.

Acknowledgement

These materials are based on work financed by the Croatian Science Foundation (HrZZ-IP-2020-02-9932 and IP-2022-10-4658 to IL, and HrZZ-IP-2019-04-8008 to NB). This work was supported by the project Centre for Advanced Laser Techniques (CALT), co-funded by the European Union through the European Regional Development Fund under the Competitiveness and Cohesion Operational Program (Grant No. KK.01.1.1.05.0001). The authors thank Dr. Iva Džeba from the RBI for the LFP measurements.

References:

[1] Kolb, H. C.; Finn, M. G.; Sharpless, K. B. Click Chemistry: Diverse Chemical Function from a Few Good Reactions. *Angew. Chem. Int. Ed*. **2001**, *40*, 2004-2021.
[2] Kumar, G. S.; Lin, Q. Light-Triggered Click Chemistry. *Chem. Rev*. **2021**, *121*, 6991-7031.
[3] Shieh, P.; Hill, M. R.; Zhang, W.; Kristufek, S. L.; Johnson, J. A. Clip Chemistry: Diverse (Bio)(macro)molecular and Material Function through Breaking Covalent Bonds. *Chem. Rev*. **2021**, *121*, 7059-7121.
[4] Lerch, M. M.; Hansen, M. J.; van Dam, G. M.; Szymanski, W.; Feringa, B. L. Emerging Targets in Photopharmacology. *Angew. Chem. Int. Ed*. **2016**, *55*, 10978-10999.
[5] Hüll, K.; Morstein, J.; Trauner, J. *In Vivo* Photopharmacology. *Chem. Rev.* **2018**, *118*, 10710-10747.
[6] Bochet, C. G. Photolabile protecting groups and linkers. *J. Chem. Soc*., *Perkin Trans.1*, **2002**, 125-142.
[7] Pelliccioli, A. P.; Wirz, J. Photoremovable protecting groups: reaction mechanisms and applications. *Photochem. Photobiol. Sci.* **2002**, *1*, 441-458.

[8] Bochet, C. G., Photochemical release of various functional groups. *Pure Appl. Chem.* **2006**, *78*, 241-247.
[9] Bochet, C. G.; Blanc, A., Photolabile Protecting Groups in Organic Synthesis. in Handbook of Synthetic Photochemistry, Albini, A.; Fagnoni, M., Eds., Wiley-VCH, Weinheim, 2010, p. 417-447.
[10] Bochet, C. G., Blanc, A. Photolabile Protecting Groups in Organic Synthesis. in CRC Handbook of Organic Photochemistry and Photobiology, Griesbeck, A.G.; Oelgemöller, M.; Ghetti, F., Eds., CRC Press, Boca Raton, 2012, p. 73-93.
[11] Wang, P. Photolabile Protecting Groups: Structure and Reactivity. *Asian J. Org. Chem.* **2013**, *2*, 452-464.
[12] Klan, P.; Šolomek, T.; Bochet, C. G.; Blanc, A.; Givens, R.; Rubina, M.; Popik, V.; Kostikov, A.; Wirz, J. Photoremovable Protecting Groups in Chemistry and Biology: Reaction Mechanisms and Efficacy. *Chem.Rev.* **2013**, *113*, 119-191.
[13] Šolomek, T.; Wirz, J.; Klán, P. Searching for Improved Photoreleasing Abilities of Organic Molecules. *Acc. Chem. Res.* **2015**, *48*, 3064-3072.
[14] Wang, P. Developing photolabile protecting groups based on the excited state meta effect. *J. Photochem. Photobiol. A: Chem.* **2017**, *335*, 300-310.
[15] Weinstain, R.; Slanina, T.; Kand, D.; Klán, P. Visible-to-NIR-Light Activated Release: From Small Molecules to Nanomaterials. *Chem. Rev*. **2020**, *120*, 13135-13272.
[16] Ellis-Davies, G. C. R. Reverse Engineering Caged Compounds: Design Principles for their Application in Biology. *Angew Chem Int. Ed*. **2023**, *62*, e202206083.
[17] Shrestha, P.; Kand, D.; Weinstain, R.; Winter, A. H. *meso*-Methyl BODIPY Photocages: Mechanisms, Photochemical Properties, and Applications. *J. Am. Chem. Soc*. **2023**, *145*, 17497-17514.
[18] Singh, P. K.; Majumdar, P.; Singh, S. P. Advances in BODIPY photocleavable protecting groups, *Coord Chem Rev*. **2021**, *449*, 214193.
[19] Toupin, N. P.; Arora, K.; Shrestha, P.; Peterson, J. A.; Fischer, L. J.; Rajagurubandara, E.; Podgorski, I.; Winter, A. H.; Kodanko, J. J. BODIPY-Caged Photoactivated Inhibitors of Cathepsin B Flip the Light Switch on Cancer Cell Apoptosis. *ACS Chem. Biol*. **2019**, *14*, 2833-2840.
[20] Sitkowska, K.; Hoes, M. F.; Lerch, M. M.; Lameijer, L. N.; Van Der Meer, P.; Szymański, W.; Feringa, B. L. Red-light-sensitive BODIPY photoprotecting groups for amines and their biological application in controlling heart rhythm. *Chem. Commun*. **2020**, *56*, 5480-5483.
[21] Wijesooriya, C. S.; Peterson, J. A.; Shrestha, P.; Gehrmann, E. J.; Winter, A. H.; Smith, E. A. A Photoactivatable BODIPY Probe for Localization-Based Super-Resolution Cellular Imaging. *Angew. Chem. Int. Ed*. **2018**, *57*, 12685-12689.
[22] Kand, D.; Pizarro, L.; Angel, I.; Avni, A.; Friedmann-Morvinski, D.; Weinstain, R. Organelle-Targeted BODIPY Photocages: Visible-Light-Mediated Subcellular Photorelease. *Angew. Chem. Int. Ed*. **2019**, *58*, 4659-4663.
[23] Kand, D.; Liu, P.; Navarro, M. X.; Fischer, L. J.; Rousso-Noori, L.; Friedmann-Morvinski, D.; Winter, A. H.; Miller, E. W.; Weinstain, R. Water-Soluble BODIPY Photocages with Tunable Cellular Localization. *J. Am. Chem. Soc.* **2020**, *142*, 4970-4974.
[24] Poryvai, A.; Galkin, M.; Shvadchak, V.; Slanina, T. Red-Shifted Water-Soluble BODIPY Photocages for Visualisation and Controllable Cellular Delivery of Signaling Lipids. *Angew. Chem. Int. Ed*. **2022**, *61*, e202205855.
[25] Haugland, R. P. The Handbook. A Guide to Fluorescent Probes and Labeling Technologies, 10th ed.; Molecular Probes, Inc.: Eugene, Oregon, USA, 2005.
[26] Treibs, A.; Kreuzer, F.-H. Difluorboryl□Komplexe von Di□ und Tripyrrylmethenen. *Liebigs Ann. Chem*. **1968**, 718, 208-223.

[27] Loudet, A.; Burgess, K. BODIPY Dyes and Their Derivatives: Syntheses and Spectroscopic Properties. *Chem. Rev*. **2007**, 107, 4891-4932.
[28] Ulrich, G.; Ziessel, R.; Harriman, A. The chemistry of fluorescent BODIPY dyes: versatility unsurpassed. *Angew. Chem. Int. Ed*. **2008**, *47*, 1184-1201.
[29] Boens, N.; Verbelen, B.; Ortiz, M. J.; Jiao, L.; Dehaen, W. Synthesis of BODIPY dyes through postfunctionalization of the boron dipyrromethene core. *Coord. Chem. Rev.* **2019**, *399*, 213024.
[30] Bumagina, N. A.; Antina, E. V.; Ksenofontov, A. A.; Antina, L. A.; Kalyagin, A. A.; Berezin, M. B. Basic structural modifications for improving the practical properties of BODIPY. *Coord. Chem. Rev*. **2022**, *469*, 214684.
[31] Rubinstein, N.; Liu, P.; Miller, E. W.; Weinstain, R. *meso*-Methylhydroxy BODIPY: a scaffold for photo-labile protecting groups. *Chem. Commun*. **2015**, *51*, 6369-6372.
[32] Goswami, P. P.; Syed, A.; Beck, C. L.; Albright, T. L.; Mahoney, K. M.; Unash, R.; Smith, E. A.; Winter, A. H. BODIPY-Derived Photoremovable Protecting Groups Unmasked with Green Light. *J. Am. Chem. Soc*. **2015**, *137*, 3783-3786.
[33] Dissanayake, K. C.; Yuan, D.; Winter, A. H., Structure-Photoreactivity Studies of BODIPY Photocages: Limitations of the Activation Barrier for Optimizing Photoreactions. *J. Org. Chem.* **2024**, *89*, 6740-6748.
[34] Buck, A. T.; Beck, C. L.; Winter, A. H. Inverted Substrate Preferences for Photochemical Heterolysis Arise from Conical Intersection Control. *J. Am. Chem. Soc*. **2014**, *136*, 8933-8940.
[35] Slanina, T.; Shrestha, P.; Palao, E.; Kand, D.; Peterson, J. A.; Dutton, A. S.; Rubinstein, N.; Weinstain, R.; Winter, A. H.; Klán, P. In Search of the Perfect Photocage: Structure-Reactivity Relationships in *meso*-Methyl BODIPY Photoremovable Protecting Groups. *J. Am. Chem. Soc*. **2017**, *139*, 15168-15175.
[36] Shrestha, P.; Dissanayake, K. C.; Gehrmann, E. J.; Wijesooriya, C. S.; Mukhopadhyay, A.; Smith, E. A.; Winter, A. H. Efficient Far-Red/Near-IR Absorbing BODIPY Photocages by Blocking Unproductive Conical Intersections. *J. Am. Chem. Soc*. **2020**, *142*, 15505-15512.
[37] Shrestha, P.; Mukhopadhyay, A.; Dissanayake, K. C.; Winter, A. H. Efficiency of Functional Group Caging with Second-Generation Green- and Red-Light-Labile BODIPY Photoremovable Protecting Groups. *J. Org. Chem*. **2022**, *87*, 14334-14341.
[38] Peterson, J. A.; Wijesooriya, C.; Gehrmann, E. J.; Mahoney, K. M.; Goswami, P. P.; Albright, T. R.; Syed, A.; Dutton, A. S.; Smith, E. A.; Winter, A. H. Family of BODIPY Photocages Cleaved by Single Photons of Visible/Near-Infrared Light. *J. Am. Chem. Soc*. **2018**, *140*, 7343-7346.
[39] Palao, E.; Slanina, T.; Muchová, L.; Šolomek, T.; Vítek, L.; Klán, P. Transition-Metal-Free CO-Releasing BODIPY Derivatives Activatable by Visible to NIR Light as Promising Bioactive Molecules. *J. Am. Chem. Soc*. **2016**, *138*, 126-133.
[40] Štacko, P.; Muchová, L.; Vítek, L.; Klán, P. Visible to NIR Light Photoactivation of Hydrogen Sulfide for Biological Targeting. *Org. Lett*. **2018**, *20*, 4907-4911.
[41] Peterson, J. A.; Fischer, L. J.; Gehrmann, E. J.; Shrestha, P.; Yuan, D.; Wijesooriya, C. S.; Smith, E. A.; Winter, A. H. Direct Photorelease of Alcohols from Boron-Alkylated BODIPY Photocages. *J. Org. Chem*. **2020**, *85*, 5712-5717.
[42] Sitkowska, K.; Feringa, B. L.; Szymański, W. Green-Light-Sensitive BODIPY Photoprotecting Groups for Amines, *J. Org. Chem.* **2018**, *83*, 1819-1827.
[43] Sambath, K.; Zhao, T.; Wan, Z.; Zhang, Y. Photo-uncaging of BODIPY oxime ester for histone deacetylases induced apoptosis in tumor cells. *Chem. Commun*., **2019**, *55*, 14162-14165.

[44] Gong, Q.; Zhang, X.; Li, W.; Guo, X.; Wu, Q.; Yu, C.; Jiao, L.; Xiao, Y.; Hao, E. Long-Wavelength Photoconvertible Dimeric BODIPYs for Super-Resolution Single-Molecule Localization Imaging in Near-Infrared Emission. *J. Am. Chem. Soc*. **2022**, *144*, 21992-21999.
[45] Li, H.; Zhang, Q.; Guo, X.; Bu, W.; Zuo, H.; Jiao, L.; Li, Z.; Yu, C.; Wang, S.; Hao, E. Dual-Color Photoconvertible BODIPY Dyes Based on Visible-Light Photouncaging of Nitrobenzyl Moieties for Living-Cell Imaging. *Adv. Optical Mater*. **2024**, *12*, 2302014.
[46] Zlatić, K.; Popović, M.; Uzelac, L.; Kralj; M.; Basarić, N. Antiproliferative activity of meso-substituted BODIPY photocages: Effect of electrophiles vs singlet oxygen. *Eur. J. Med. Chem.* **2023**, *259*, 115705.
[47] Kawatani, M.; Kamiya, M.; Takahashi, H.; Urano, Y. Factors affecting the uncaging efficiency of 500 nm light-activatable BODIPY caging group. *Bioorg. Med. Chem. Lett*. **2018**, *28*, 1-5.
[48] Sharma, A. K.; Nair, M.; Chauhan, P.; Gupta, K.; Saini, D. K.; Chakrapani, H., Visible-Light-Triggered Uncaging of Carbonyl Sulfide for Hydrogen Sulfide (H_2S) Release. *Org. Lett*. **2017**, *19*, 4822-4825.
[49] Umeda, N.; Takahashi, H.; Kamiya M.; Ueno, T.; Komatsu, T.; Terai, T.; Hanaoka, K.; Nagano, T.; Urano, Y. Boron Dipyrromethene As a Fluorescent Caging Group for Single-Photon Uncaging with Long-Wavelength Visible Light. *ACS Chem. Biol*. **2014**, *9*, 2242-2246.
[50] Ader, R.; Loewenstein, A. Proton and deuteron magnetic resonance of methanes, silanes and GeH_3D dissolved in nematic liquid crystals Part I. Experimental results. *Mol. Phys*. **1975**, *30*, 199-208.
[51] Bernheim, R. A.; Lavery, B. J. Isotope shift in the proton magnetic resonance of CH_4, CH_3D, CH_2D_2, and CHD_3. *J. Chem. Phys*. **1965**, *42*, 1464.
[52] Anet, F. A. L.; O'Leary, D. J. H-D Coupling Constants and Deuterium Isotope Effects on the Proton Chemical Shifts in Partially Deuteriated Methanes. *Tetrahedron Lett*. **1989**, *30*, 2755-2758.
[53] Carmichael, I.; Hug, G. L. Triplet–Triplet Absorption Spectra of Organic Molecules in Condensed Phases, *J. Phys. Chem. Ref. Data*. **1986**, *15*, 1-250.
[54] van Leeuwen, M.; Beeby, A.; Fernandes, I.; Ashworth, S. H. The photochemistry and photophysics of a series of alpha octa(alkyl-substituted) silicon, zinc and palladium phthalocyanines, *Photochem. Photobiol. Sci*. **2014**, *13*, 62-69.
[55] Tran Thi, T. H.; Thiec, C. D. C.; Gaspard, S. Singlet-singlet and triplet-triplet intramolecular transfer processes in a covalently linked porphyrin-phthalocyanine heterodimer. *J. Phys. Chem.* **1989**, *93,* 1226-1233.
[56] Boens, N.; Qin, W.; Basarić, N.; Hofkens, J.; Ameloot, M.; Pouget, J.; Lefèvre, J. P.; Valeur, B.; Gratton, E.; VandeVen, M.; Silva, N. D.; Engelborghs, Y.; Willaert, K.; Sillen, A.; Rumbles, G.; Phillips, D.; Visser, A. J. W. G.; Van Hoek, A.; Lakowicz, J. R.; Malak, H.; Gryczynski, I.; Szabo, A. G.; Krajcarski, D. T.; Tamai, N.; Miura, A. Fluorescence Lifetime Standards for Time and Frequency Domain Fluorescence Spectroscopy. *Anal. Chem*. **2007**, *79*, 2137-2149.
[57] Huynh, M. H. V.; Meyer, T. J. Colossal kinetic isotope effects in proton-coupled electron transfer. *PNAS*, **2004**, *101*, 13138-13141.
[58] Momeni, M. R.; Brown, A., Why Do TD-DFT Excitation Energies of BODIPY/Aza-BODIPY Families Largely Deviate from Experiment? Answers from Electron Correlated and Multireference Methods, *J. Chem. Theory Comput*. **2015**, *11*, 2619-2632.
[59] Nykänen, A.; Thiessen, L.; Borrelli, E.-M.; Krishna, V.; Knecht, S.; Pavošević, F., Toward Accurate Calculation of Excitation Energies on Quantum Computers with ΔADAPT-VQE: A Case Study of BODIPY Derivatives, *J. Phys. Chem. Lett*. **2024**, *15*, 7111-7117.

[60] Qin, W.; Baruah, M.; Van der Auweraer, M.; De Schryver, F. C.; Boens, N. Photophysical Properties of Borondipyrromethene Analogues in Solution. *J. Phys. Chem. A* **2005**, *109*, 7371-7384.
[61] Kee, H. L.; Kirmaier, C.; Yu, L. H.; Thamyongkit, P.; Youngblood, W. J.; Calder, M. E.; Ramos, L.; Noll, B. C.; Bocian, D. F.; Scheidt, W. R.; Birge, R. R.; Lindsey, J. S.; Holten, D., Structural Control of the Photodynamics of Boron-Dipyrrin Complexes, *J. Phys. Chem. B* **2005**, *109*, 20433-20443.
[62] Dent, M. R.; López-Duarte, I.; Dickson, C. J.; Geoghegan, N. D.; Cooper, J. M.; Gould, I. R.; Krams, R.; Bull, J. A.; Brooks, N. J.; Kuimova, M. K., Imaging phase separation in model lipid membranes through the use of BODIPY based molecular rotors. *Phys. Chem. Chem. Phys.* **2015**, *17*, 18393-18402.
[63] Lincoln, R.; Greene, L. E.; Bain, C.; Flores-Rizo, J. O.; Bohle, D. S.; Cosa, G., When Push Comes to Shove: Unravelling the Mechanism and Scope of Nonemissive meso-Unsaturated BODIPY Dyes. *J. Phys. Chem. B* **2015**, *119*, 4758-4765.
[64] Suhina, T.; Amirjalayer, S.; Woutersen, S.; Bonn, D.; Brouwer, A. M., Ultrafast dynamics and solvent-dependent deactivation kinetics of BODIPY molecular rotors. *Phys. Chem. Chem. Phys*. **2017**, *19*, 19998-20007.
[65] Glavaš, M.; Zlatić, K.; Jadreško, D.; Ljubić, I.; Basarić, N., Fluorescent pH sensors based on BODIPY structure sensitive in acidic media, *Dyes and Pigments* **2023**, *220*, 111660.
[66] Rieckhoff, K. E.; Menzel, E. R.; Voigt, E. M., Molecular Fluorescence from High Vibrational Levels of Excited Electronic States, *Phys. Rev. Lett*. **1972**, *28*, 261-263.
[67] Osuna, S.; Swart, M.; Baerends, E. J.; Bickelhaupt, F. M.; Sola, M., Homolytic versus Heterolytic Dissociation of Alkalimetal Halides: The Effect of Microsolvation, *Chem. Phys. Chem.* **2009**, *10*, 2955-2965.
[68] Hoyer, C. E.; Xu, X.; Ma, D.; Gagliardi, L.; Truhlar, D. G., Diabatization based on the dipole and quadrupole: The DQ method, *J. Chem. Phys*. **2014**, *141*, 114104.
[69] Sviben, I.; Džeba, I.; Bonifačić, M.; Ljubić, I., Kinetics of chain reaction driven by proton-coupled electron transfer: α-hydroxyethyl radical and bromoacetate in buffered aqueous solutions, *Phys. Chem. Chem. Phys*., **2021**, *23*, 10429-10439.
[70] Gräfenstein, J.; Cremer, D. The self-interaction error and the description of non-dynamic electron correlation in density functional theory, *Theor. Chem. Acc*. **2009**, *123*, 171-182.
[71] Bao, J. L.; Gagliardi, L.; Truhlar, D. G., Self-Interaction Error in Density Functional Theory: An Appraisal, *J. Phys. Chem. Lett*. **2018**, *9*, 2353-2358.
[72] Fischer, L. J.; Dutton, A. S.; Winter, A. H., Anomalous effect of non-alternant hydrocarbons on carbocation and carbanion electronic configurations, *Chem. Sci*., **2017**, 8, 4231-4241.
[73] For the output of the cool white lamp see the info. from the Luzchem provider: https://cdn.shopify.com/s/files/1/0823/1560/8376/files/LESVIS019.pdf?v=1695047226 web-site accessed on October 23, 2024.
[74] Roos, B. O.; Lindh, R.; Malmqvist, P. Å.; Veryazov, V.; Widmark, P. O., Multiconfigurational Quantum Chemistry, John Wiley & Sons Inc., Hoboken, New Jersey, 2016.
[75] Andersson, K.; Malmqvist, P. Å.; Roos, B. O., Second-order perturbation theory with a complete active space self-consistent field reference function, *J. Chem. Phys*., **1992**, *96*, 1218-1226.
[76] Becke, A. D. Density□functional thermochemistry. III. The role of exact exchange, *J. Chem. Phys*., **1993**, *98*, 5648-5652.

[77] Stephens, P. J.; Devlin, F. J.; Chablowski, C. F.; Frisch, M. J., Ab Initio Calculation of Vibrational Absorption and Circular-Dichroism Spectra Using Density-Functional Force-Fields. *J. Phys. Chem*., **1994**, *98*, 11623-11627.
[78] Vosko, S. H.; Wilk, L.; Nusair, M., Accurate Spin-Dependent Electron Liquid Correlation Energies for Local Spin Density Calculations: A Critical Analysis, *Can. J. Phys*. **1980**, *58*, 1200-1211.
[79] Yanai, T., Tew, D., Handy, N., A new hybrid exchange–correlation functional using the Coulomb-attenuating method (CAM-B3LYP), *Chem. Phys. Lett*. **2004**, *393*, 51-57.
[80] Mandić, L.; Ljubić, I.; Džeba, I., Time-resolved spectroscopic and computational study of the initial events in doxazosin photochemistry, *Spectrochim. Acta A*, **2024**, *306*, 123595.
[81] Nikšić-Franjić, I.; Ljubić, I., Comparing the performances of various density functionals for modelling the mechanisms and kinetics of bimolecular free radical reactions in aqueous solution, *Phys. Chem. Chem. Phys*., **2019**, *21*, 23425-23440.
[82] Yua, L.J.; Dale, S. G.; Chan, B.; Karton, A., Benchmark study of DFT and composite methods for bond dissociation energies in argon compounds, *Chem. Phys*., **2020**, *531*, 110676.
[83] Tomasi, J.; Mennucci, B.; Cammi, R., Quantum mechanical continuum solvation models, *Chem. Rev*., **2005**, *105*, 2999-3093.
[84] Cossi, M.; Scalmani, G.; Rega, N.; Barone, V., New developments in the polarizable continuum model for quantum mechanical and classical calculations on molecules in solution, *J. Chem. Phys*., **2002**, *117*, 43-54.
[85] Grimme, S.; Antony, J.; Ehrlich, S.; Krieg, H., A consistent and accurate ab initio parameterization of density functional dispersion correction (DFT-D) for the 94 elements H-Pu, *J. Chem. Phys*., **2010**, *132*, 154104.
[86] Dunning, T. H. Jr., Gaussian basis sets for use in correlated molecular calculations. I. The atoms boron through neon and hydrogen, *J. Chem. Phys*., **1989**, *90*, 1007-1023.
[87] Ghigo, G.; Roos, B. O.; Malmqvist, P. Å., A modified definition of the zeroth-order Hamiltonian in multiconfigurational perturbation theory (CASPT2), *Chem. Phys. Lett*., **2004**, *396*, 142-149.
[88] Forsberg, N.; Malmqvist, P. Å., Multiconfiguration perturbation theory with imaginary level shift, *Chem. Phys. Lett*., **1997**, *274*, 196-204.
[89] Cossi, M.; Rega, N.; Scalmani, G.; Barone, V., Energies, structures, and electronic properties of molecules in solution with the C-PCM solvation model, *J. Comput. Chem*. **2003**, *24*, 669-681.
[90] Santoro, F.; Lami, A.; Improta, R.; Bloino, J.; Barone, V., Effective method for the computation of optical spectra of large molecules at finite temperature including the Duschinsky and Herzberg-Teller effect: the Qx band of porphyrin as a case study. *J. Chem. Phys*., **2008**, *128*, 224311.
[91] Gaussian 16, Revision C.01, M. J. Frisch et al., Gaussian, Inc., Wallingford CT, 2016.
[92] Galván, F. I. et al. OpenMolcas: From Source Code to Insight. *J. Chem. Theory Comput*. **2019**, *15*, 5925-5964.
[93] Boto, R. A.; Peccati, F.; Laplaza, R.; Quan, C.; Carbone, A.; Piquemal, J.-P.; Maday, Y.; Contreras-García, J., NCIPLOT4: Fast, Robust, and Quantitative Analysis of Noncovalent Interactions, *J. Chem. Theory Comput*. **2020**, *16*, 4150-4158.